Contributions to Mineralogy and Petrology (2026) 181:62
https://doi.org/10.1007/s00410-026-02341-w

ORIGINAL PAPER

High-pressure phase relations in the Mg–Fe–O system and the conditions at which ferropericlase inclusions in diamonds are formed

Caterina Melai[1] · Daniel J. Frost[1] · Tiziana Boffa Ballaran[1] · Catherine A. McCammon[1] · Nobuyoshi Miyajima[1] · Lin Wang[1,2]

Received: 17 February 2026 / Accepted: 5 June 2026 / Published online: 25 July 2026
© The Author(s) 2026

Abstract

Constraints can be placed on the formation conditions of $(Mg,Fe)_XO$ ferropericlase inclusions in natural diamonds based on their Fe^{3+} contents, given suitable knowledge of how these contents change with pressure, temperature, composition and oxygen fugacity. To achieve this, experiments have been conducted to determine the maximum Fe^{3+}/Fe_{tot} ratio in ferropericlase, controlled by its coexistence with magnetite–magnesioferrite (Fe_3O_4–$MgFe_2O_4$) up to pressures of ~ 6 GPa, and with the high-pressure $[Fe,Mg]_2Fe_2O_5$ phase between 10 and 30 GPa. The experiments were performed between 1200 and 1800 °C and across a range of bulk Fe/(Fe + Mg) ratios. Mössbauer and electron energy loss spectroscopy were used to determine ferropericlase Fe^{3+}/Fe_{tot} ratios, a task that is complicated by exsolution of nanocrystalline magnetite–magnesioferrite during quenching. Using these data, a thermodynamic model was developed that describes the entire range of ferropericlase compositions in the Mg–Fe–O system between 1 atmosphere and 30 GPa. It is shown that the Fe^{3+}/Fe_{tot} ratio of ferropericlase within diamond-forming assemblages decreases strongly above 10 GPa, and that the majority of ferropericlase inclusions in diamonds with measured Fe^{3+}/Fe_{tot}, have ratios too high for them to have formed in the lower mantle. Most of these ferropericlase inclusions have maximum formation depths in the transition zone, but a few of the most oxidised could only have formed in the upper mantle from oxidised precursors such as carbonates. We also show that high pressure $(Fe,Mg)_2Fe_2O_5$ and $(Fe,Mg)_3Fe_2O_6$ phases can become stable during diamond formation towards the base of the transition zone, when bulk Fe/(Fe + Mg) ratios are > 0.5.

Keywords High-pressure · Mantle · Oxygen fugacity · Ferric iron

Introduction

Ferropericlase (fper) is likely to be the second most abundant mineral in the Earth's lower mantle and is also found as inclusions in superdeep diamonds, which are proposed to originate at sub-lithospheric conditions. In fact, fper inclusions are used to identify superdeep diamonds as such and, in many instances, it is argued that they originate in the lower mantle (Scott Smith et al. 1984; Harte 1994; Harte et al. 1999; Stachel et al. 2000; Kaminsky et al. 2001; Kaminsky 2012; Walter et al. 2022; Lorenzon et al. 2023; Ni et al. 2025). A lower mantle origin assumes that the inclusions were formed in equilibrium with a typical mantle assemblage, however, fper inclusions could, in principle, form from silica-poor compositions at practically any depth in the diamond stability field (Gurney 1989; Stachel et al. 1998; Brey et al. 2004; Bulatov et al. 2019).

The wüstite-periclase (FeO-MgO) solid solution, which we refer to here for simplicity as fper, can also contain a significant fraction of Fe^{3+}, the incorporation of which is charge balanced through the creation of metal cation vacancies (V), described by the formula $Mg_zFe^{2+}_{1-z-3x}Fe^{3+}_{2x}V_xO$. At room pressure the Fe^{3+}/Fe_{tot} ratio of fper varies strongly with oxygen fugacity (fO_2), reaching a minimum where fper is in equilibrium with iron metal (Srečec et al. 1987; O'Neill et al. 2003) and a maximum where it coexists with spinel phases

Communicated by Dante Canil.

✉ Daniel J. Frost
dan.frost@uni-bayreuth.de

[1] Bayerisches Geoinstitut, Universität Bayreuth, 95440 Bayreuth, Germany

[2] Current address, State Key Laboratory of Critical Mineral Research and Exploration, Institute of Geochemistry, Chinese Academy of Sciences, Guiyang, China

along the magnetite-magnesioferrite (Fe_3O-$MgFe_2O_4$) solid solution (Brynestad and Flood 1958; Katsura and Kimura 1965; Speidel 1967; Hilbrandt and Martin 1998). Several studies have proposed using the Fe^{3+}/Fe_{tot} ratio of fper inclusions in diamonds to determine the fO_2 at which such inclusions formed (Longo et al. 2011; Otsuka et al. 2013; Kaminsky et al. 2015). Otsuka et al. (2013) used the results of high-pressure experiments to calibrate an equation for the Fe^{3+} content of fper as a function of MgO content, P, T, and fO_2. However, this calibration is based on a relatively small data set, which does not extend to conditions that define the fper stability field at high fO_2.

Several studies have also noted that fper inclusions in diamonds can contain nano- to micro-sized exsolutions of magnetite-magnesioferrite spinel phases, hereafter abbreviated as spft (Harte et al. 1999; Wirth et al. 2014; Kaminsky et al. 2015; Nestola et al. 2016; Palot et al. 2016; Nimis et al. 2019; Anzolini et al. 2020; Kiseeva et al. 2022). Wirth et al. (2014), for example, found nanometre-scale coherent spft exsolution in $Mg_{0.35}Fe_{0.65}O$ fper inclusions. As this exsolution in fper most likely occurred after entrapment, the composition and proportion of the exsolving phase must be known to reconstruct the initial fper Fe^{3+}/Fe_{tot} ratio upon entrapment (Wirth et al. 2014; Kaminsky et al. 2015). Kaminsky et al. (2015), for example, found that on average the Fe^{3+}/Fe_{tot} ratio measured by Mössbauer spectroscopy for fper inclusions found in several diamonds, needed to be increased by ~ 0.021 to account for the presence of spft exsolution.

Aside from influencing the Fe^{3+}/Fe_{tot} ratio of fper inclusions in diamonds, the question remains as to when such exsolution occurs and whether this reflects changes in P or T, or possibly even fO_2, after entrapment. To address this, information is required on the conditions at which fper becomes saturated in Fe^{3+}, which is presumably what causes the spft to form. Furthermore, the conditions and Fe^{3+}/Fe_{tot} ratios of fper when it is in equilibrium with spft would provide excellent constraints on fper thermodynamic properties in the MgO-FeO-Fe_2O_3 system, which would allow the fper stability field to be defined in terms of fO_2. Virtually no data exist, however, to constrain these properties at high pressure. A further complication is that above approximately 6 GPa, spft breaks down into a range of higher-pressure Fe–Mg oxides, such as $[Mg, Fe]_2^{2+}Fe_2^{3+}O_4$ and $[Mg, Fe]_3^{2+}Fe_2^{3+}O_6$ (Lavina et al. 2011; Woodland et al. 2012; Lavina and Meng 2015; Myhill et al. 2016; Sinmyo et al. 2016; Ishii et al. 2018), some of which may also occur as exsolutions in fper inclusions (Anzolini et al. 2020). Their stability fields remain poorly constrained, introducing uncertainty into the definition of the upper fO_2 limit of fper stability at high pressure.

In this study experiments have been performed up to pressures of 30 GPa, to determine the composition of fper, including its Fe^{3+}/Fe_{tot} ratio, at conditions where it coexists with spft, which will also be referred to as the O4 phase, or higher-pressure Fe–Mg-oxides, mainly Fe_4O_5 and $Mg_2^{2+}Fe_2^{3+}O_5$, hereafter indicated as the O5 phase. The presence of Pt-Fe alloy in the experiments was used to determine the fO_2 at the experimental P–T conditions. A thermodynamic model has been developed to fit the dataset in order to calculate the fper stability field as a function of P, T, MgO content and fO_2. In addition, this model allows the compositions of coexisting phases to be determined. The experimental dataset also includes fper samples that did not coexist with other oxides, which are used to calibrate the fper Fe^{3+}/Fe_{tot} ratio at lower fO_2. The model is used to investigate the fper stability field, the fO_2 recorded by fper inclusions in diamonds and implications for their formation conditions.

Materials and methods

Sample synthesis and characterisation

Five fper starting compositions (A to E, as given in Table 1) with nominal stoichiometries $(Mg_{0.86}Fe_{0.14})O$, $(Mg_{0.50}Fe_{0.50})O$, $(Mg_{0.30}Fe_{0.70})O$, $(Mg_{0.05}Fe_{0.95})O$ and FeO were prepared from mixtures of Fe_2O_3 and MgO, plus the minor oxides NiO (1.3 wt%), Cr_2O_3 (0.5 wt%), MnO (0.2 wt%) and Na_2O (0.05 wt%). Fe_2O_3 and MgO were pre-sintered at 1000 °C to remove volatiles. The starting powders were then ground together, pressed into pellets and then reduced for 48 h in a gas mixing furnace at 1100 °C and at an fO_2 of 2 log units below the fayalite–magnetite–quartz (FMQ) buffer. The recovered fper powders were weighed and then further ground together with 5 to 20 wt. % Fe_2O_3 powder, previously fired at 1000 °C, in order to induce the coexistence of

Table 1 Compositions of the ferropericlase starting materials in wt. %

Ferropericlase stoichiometry		Cr_2O_3	NiO	Na_2O	MnO	FeO	MgO	total	Fe_2O_3	PtO_2
$(Mg_{0.86}Fe_{0.14})O$	(A)	0.50	1.30	0.05	0.20	13.71	84.24	100	20, 10	4
$(Mg_{0.50}Fe_{0.50})O$	(B)	0.50	1.30	0.05	0.20	48.98	48.98	100	5, 20	4
$(Mg_{0.30}Fe_{0.70})O$	(C)	0.50	1.30	0.05	0.20	68.57	29.39	100	20	4
$(Mg_{0.05}Fe_{0.95})O$	(D)	0.50	1.30	0.05	0.20	93.05	4.90	100	20, 10	4
FeO	(E)	0.50	1.30	0.05	0.20	97.95	0	100	0, 5	4

The amounts of hematite and PtO_2 are given as a proportion in wt. % of the amount of ferropericlase as indicated in Table 2

spft or higher-pressure Fe–Mg-oxides in the high-pressure experiments. Additionally, 4 wt% PtO_2 powder was added to the starting materials to act as a sliding redox sensor (Woodland and O'Neill 1997; Kessel et al. 2001).

High P and T experiments were conducted using 1000- and 5000-tonne multianvil presses at the Bayerisches Geoinstitut. For pressures up to 12 GPa, 18 mm edge-length Cr_2O_3-doped MgO octahedral pressure media were used, with $LaCrO_3$ or graphite heaters depending on the conditions. The assembly was compressed using tungsten carbide cubes with 11 mm edge-length corner truncations (a so-called 18/11 assembly). For experiments performed at 16 and 25 GPa, 18/8 and 7/3 assemblies were used respectively. The starting materials were contained in Pt-foil capsules. Temperature was monitored using a W97%Re3%–W75%Re25% (D type) thermocouple inserted in an alumina tube. Experiments were first cold compressed, then heated to target temperature at a rate of 100 °C/min and then quenched by turning off the power to the furnace, with a quench rate of approximately 200–250 °C/s. Pressure calibrations are reported in Keppler and Frost (2005). A single experiment was run at 30 GPa in the IRIS -15 Voggenreiter LPH 1500–840/200 press (Ishii et al. 2017). A 5.7/1.5 assembly was used with TF05 WC anvils. In this experiment, two samples with compositions $(Mg_{0.86}Fe_{0.14})O$ and FeO were placed respectively above and below the thermocouple junction. Each sample was 0.35 mm long and was placed inside a capsule of dense Al_2O_3 tubing. The heater was comprised of 25 µm thick rhenium foil. The thermocouple was inserted longitudinally through the wall of the furnace with the junction located in the middle of the assembly. All experimental conditions are reported in Table 2.

Recovered experimental runs were cut in half with a diamond wire saw. One half was embedded in epoxy and

Table 2 Experimental starting materials, conditions and phases in the recovered run products, as determined by means of XRD and EMPA

Sample	Start. comp. + wt. % of Fe_2O_3	P (GPa)	T(°C)	Products	Sample	Start. comp. + wt. % of Fe_2O_3	P (GPa)	T(°C)	Products
S7029	A + 20%	6	1200	Fper + O_4 + Pt alloy	S7216-B	B + 20%	10	1400	Fper + Pt alloy + n-spft
Z2038	A + 20%	6	1600	Fper + Pt alloy + n-spft	S7216-A	B + 10%	10	1400	Fper + Pt alloy + n-spft
H5128	A + 20%	8	1200	Fper + Pt alloy + n-spft	Z1949-A	B + 20%	12	1200	Fper + Pt alloy + n-spft
S7004	A + 20%	8	1200	Fper + Pt alloy + n-spft	Z2122-B	B + 20%	16	1200	Fper + O_5 + Pt alloy
S7377	A + 20%	10	1200	Fper + O_4 + Pt alloy	Z2117-B	B + 20%	17	1200	Fper + O_5 + Pt alloy
S7180	A + 20%	10	1600	Fper + Pt alloy + n-spft	Z2115-B	B + 20%	20	1200	Fper + O_5 + Pt alloy
S7204	A + 20%	10	1800	Fper + Pt alloy + n-spft	Z2121-A	B + 20%	20	1600	Fper + O_5 + Pt alloy
Z1949-B	A + 20%	12	1200	Fper + Pt alloy + n-spft	Z2151-A	B + 5%	20	1600	Fper + O_5 + Pt alloy
S7382	A + 20%	16	1200	Fper + O_5 + Pt alloy	Z2153-A	B + 5%	20	1800	Fper + Pt alloy + n-spft
S7006	A + 20%	16	1200	Fper + O_5 + Pt alloy	H5189-A	C + 20%	6	1200	Fper + Pt_3Fe + n-spft
S7016	A + 20%	20	1200	Fper + O_5 + Pt alloy	S7495-A	C + 20%	10	1200	Fper + O_4 + Pt alloy
Z2151-B	A + 20%	20	1600	Fper + O_5 + Pt alloy	H5190-A	C + 20%	16	1200	Fper + O_5 + Pt alloy
Z2153-B	A + 20%	20	1800	Fper + O_5 + Pt alloy	Z2077-A	C + 20%	16	1200	Fper + O_5 + Pt alloy
H4792	A + 20%	25	1200	Fper + O_5 + Pt alloy	H5189-B	D + 20%	6	1200	Fper + O_4 + [Fper + Spft] + Pt_3Fe
S7410	A + 20%	25	1000	Fper + O_5 + Pt alloy	S7509-A	D + 20%	6	1200	Fper + O_4 + [Fper + Spft] + Pt alloy
S7123-B	A + 10%	25	1400	Fper + small O_5 # + Pt alloy	S7604-A	D + 10%	10	1200	O_5 + [Fper + Spft] + Pt alloy
I1185-A	A + 20%	30	1200	Fper + [Fper + O_4] + Pt alloy	S7495-B	D + 20%	10	1200	O_6 + Pt_3Fe
S7470	B + 20%	6	1200	Fper + Pt alloy	Z2122-A	D + 20%	16	1200	O_6 + Pt_3Fe
H5164	B + 20%	6	1200	Fper + Pt alloy	Z2115-A	D + 20%	20	1200	O_6 + Pt_3Fe
S7510	B + 20%	6	1600	Fper + Pt_3Fe + n-spft	Z2077-B	D	16	1200	O_6 + Pt_3Fe
S7509-B	B + 20%	6	1200	Fper + Pt_3Fe + n-spft	H5190-B	D	16	1200	O_6 + Pt_3Fe
S7716-B	B + 5%	6	1200	Fper + Pt alloy + n-spft	Z2117-A	D + 20%	17	1200	O_6 + Pt_3Fe
Z2116	B + 20%	8	1200	Fper + Pt alloy + n-spft	Z2120-A	D + 20%	17	1200	O_6 + Pt_3Fe
S7691-A	B + 5%	8	1200	Fper + Pt alloy + n-spft	S7716 A	E	6	1200	[FeO + Fe_3O_4] + Pt_3Fe
Z2155-B	B	8	1200	Fper + Pt alloy + n-spft	S7691-B	E	8	1200	[FeO + Fe_3O_4] + Pt_3Fe
Z2155 A	B + 5%	8	1200	Fper + Pt_3Fe + n-spft	I1185-B	E	30	1200	FeO + Fe_5O_6 + Pt alloy

Phases in square brackets have formed through decomposition. * broad peaks in the X-ray patters of samples showing no macroscopic spinel phase are fit with $(Mg,Fe)Fe_2O_4$ and called n-spft. Squared parentheses indicate back transformation products. # no O_5 detected in XRD; $O_4 = (Mg,Fe)Fe_2O_4$; $O_5 = (Mg,Fe)_2Fe_2O_5$; $O_6 = (Mg,Fe)_3Fe_2O_6$

polished for electron microprobe analyser (EPMA), scanning electron microscope (SEM) and powder X-ray diffraction (XRD) measurements. The other half was polished to a thickness varying between 250 and 200 µm, depending on the iron content of the sample (Long et al. 1983), for Mössbauer spectroscopy (MS) measurements. Textural observations were performed using an SEM (ZEISS Gemini 1530). Quantitative chemical compositions of the mineral phases were obtained using EMPA (JEOL JXA 8200) operating at an acceleration voltage of 15 kV and beam current of 15 nA. The Phi-rho-Z correction routine was applied for all analyses of this work. The standards employed were periclase (Mg), andradite (Fe), albite (Na), nickel oxide (Ni), $MnTiO_3$ (Mn), Cr_2O_3 (Cr) and Fe_2O_3 for O. Fe, Pt and Ni metal were used as standards for the alloy analyses. The averaged EPMA analyses for all phases present in each run product are reported in supplementary Table S1.

Powder X-ray diffraction

Phase identification was performed with a Bruker D8 DISCOVER micro-focused X-ray diffractometer (XRD) equipped with a two-dimensional solid-state detector (VANTEC500) and micro-focus Co-Ka radiation source (IµS) operated at 40 kV and 500 µA. The X-ray beam was collimated to a spot size of approximately 100 µm diameter by an IFG polycapillary X-ray mini lens. The collected X-ray patterns were integrated using the DIFFRACEVA-V3.1 package. Unit-cell parameters (Table S2) were determined through full-pattern refinements using the general structure analysis system (GSAS) software and the EXPGUI interface (Toby 2001; Larson & von Dreele 2004).

Mössbauer spectroscopy

Mössbauer spectra were acquired at room temperature in transmission mode on a constant acceleration spectrometer with a nominal 370 MBq ^{57}Co point source in a 12 µm thick Rh matrix. A piece of Ta foil drilled with a 1 mm diameter hole was used to select the area to be measured. Velocity scales were calibrated relative to 25 µm α-Fe foil. Spectra were collected using a velocity range of + 5 to -5 mms^{-1} and + 12 to – 12 mms^{-1} by moving the source relative to the sample in constant acceleration mode over 1–3 days. The wider velocity scale was dictated by the presence of magnetically ordered Fe in the run products. The resulting spectra were then folded and fitted using a pseudo-Voigt line shape and a 1st order polynomial baseline with the MossA 1.01f software package (Prescher et al. 2012). The resulting hyperfine parameters are reported in supplementary Table S3 and plotted in Fig. S1.

Fig. 1 Backscattered SEM images of samples recovered from 1200 °C and various pressures. Grains of Pt-Fe alloy (white) can be seen dispersed through all samples. **a** Sample H5128 recovered from 8 GPa, showing only the presence of fper. **b** Sample S7029 recovered from 6 GPa showing clean regions of fper (dark) coexisting with smaller grains of spft (light). **c** Sample Z2077-A (16 GPa) showing prismatic crystals of the O5 phase (light) with fper (dark). **d** Mg-free sample S7716-A (6 GPa) comprising regions dominated by wüstite (light) and magnetite (dark) with a texture indicating a back-transformation during quenching most likely from Fe_5O_6. Grain boundaries of larger pre-existing grains (~20 µm in diameter) are traced out mainly by magnetite crystals; **e** Mg-free sample I1185-B (30 GPa) consists of dark elongate crystals of Fe_5O_6 coexisting with FeO; **f** sample I1185-A (30 GPa) containing a (bright) assemblage formed through a back-transformation during quenching from a high-pressure Mg–Fe-oxide coexisting with (darker) fper that in some regions contains a visible macroscopic exsolution lamellae

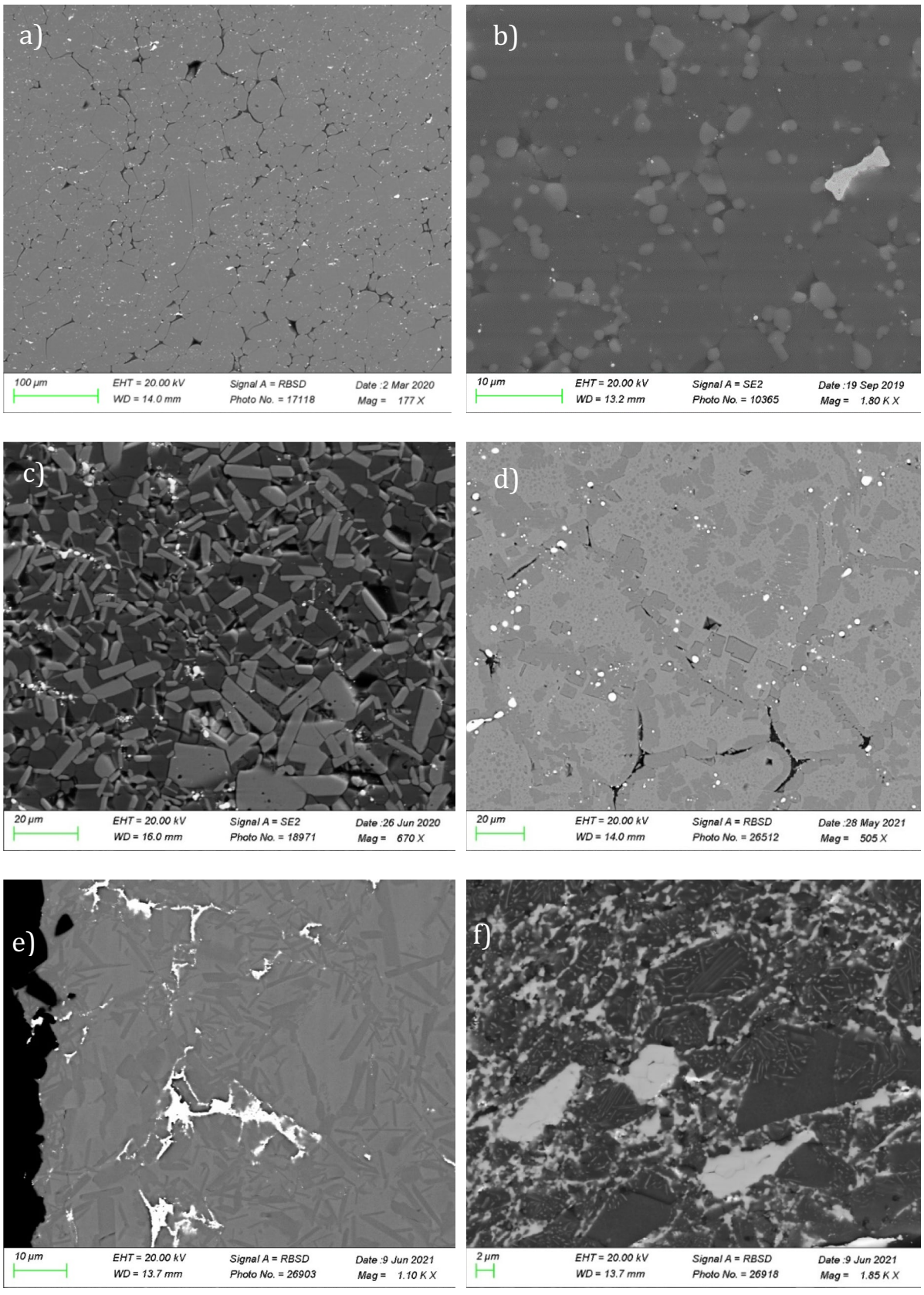
Transmission electron microscopy

Lamellae were extracted from five samples using a focused ion beam (FIB) milling machine (*FEI Scios* DualBeam) and thinned to electron transparency for Transmission Electron Microscopy (TEM) analyses. Measurements were performed using a 200 kV analytical TEM (ATEM, *FEI Titan G2 80–200 S/TEM*, *Philips CM20FEG*) equipped with an energy dispersive X-ray spectrometer (EDXS, *Brucker QUANTAX*) and an electron energy-loss spectrometer (EELS, *Gatan GIF Quantum® Model 963*). Electron energy-loss spectroscopy (EELS) measurements were performed to determine Fe^{3+}/Fe_{tot} ratios of fper and coexisting phases. The spectra were collected and treated following the procedure detailed in Melai et al., (2026).

Results

Phase relations

Most of the recovered experiments contain either fper and Fe-Pt alloy or fper, Fe-Pt-alloy and an Fe^{3+}-rich oxide (Table 2, Fig. 1). In some experiments performed at low fO_2 or with high bulk Fe/(Fe + Mg) ratios, an isoferroplatinum (Pt_3Fe) phase was detected instead of the Fe-Pt disordered alloy in the X-ray diffraction patterns. The diffraction patterns of most of the experiments in which only fper and Fe-Pt alloy were visible in the SEM images (Fig. 1a), also contain broad peaks that can be indexed to a spinel ferrite structure (Fig. 2), indicating the presence of nanoscale spft exsolutions (Longo et al. 2011), which we refer to as n-spft. N-spft reflections are even found in samples recovered from pressures at which spft is no longer stable (Table 2; Fig. 2) and its presence was confirmed by TEM analysis, as discussed later. Experiments containing only fper and Fe-Pt alloy were generally repeated with more Fe_2O_3 added to


a)
100 µm
EHT = 20.00 kV
WD = 14.0 mm
Signal A = RBSD
Photo No. = 17118
Date :2 Mar 2020
Mag = 177 X
b)
10 µm
EHT = 20.00 kV
WD = 13.2 mm
Signal A = SE2
Photo No. = 10365
Date :19 Sep 2019
Mag = 1.80 K X
c)
20 µm
EHT = 20.00 kV
WD = 16.0 mm
Signal A = SE2
Photo No. = 18971
Date :26 Jun 2020
Mag = 670 X
d)
20 µm
EHT = 20.00 kV
WD = 14.0 mm
Signal A = RBSD
Photo No. = 26512
Date :28 May 2021
Mag = 505 X
e)
10 µm
EHT = 20.00 kV
WD = 13.7 mm
Signal A = RBSD
Photo No. = 26903
Date :9 Jun 2021
Mag = 1.10 K X
f)
2 µm
EHT = 20.00 kV
WD = 13.7 mm
Signal A = RBSD
Photo No. = 26918
Date :9 Jun 2021
Mag = 1.85 K X

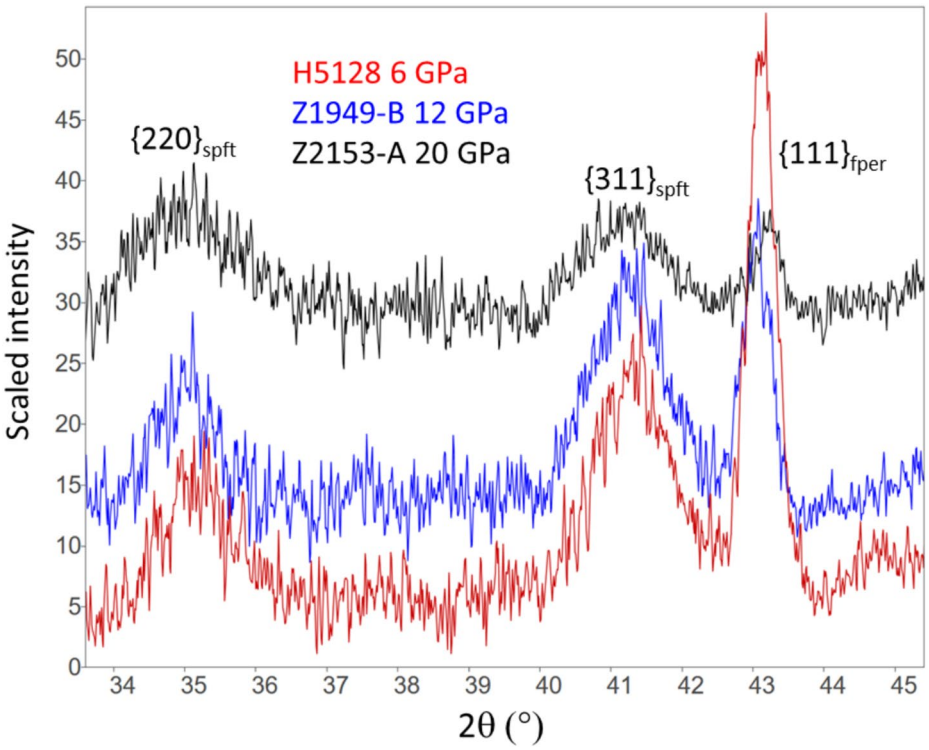


Fig. 2 Details of the X-ray powder diffraction patterns collected for samples recovered from 1200 °C and the pressures indicated and containing only macroscopic fper and Pt-Fe alloy. The broad peaks can be assigned to the {220} and {311} reflections of the spft structure even in samples from 12 and 20 GPa where spft should no longer be stable. The broadening of the peaks with pressure implies increasingly smaller particle sizes

the starting material until an additional Fe^{3+}-rich phase was formed.

The O5 ($[Mg,Fe]_2Fe_2O_5$) and O6 phases ($[Mg,Fe]_3Fe_2O_6$) were identified in the samples using XRD. In one instance (S7123-B), EPMA, including oxygen measurements, were used to identify a small amount of the O5 phase that did not appear in the XRD pattern. Samples produced close to the transformation of spft to the O5 phase at approximately 6 GPa show evidence of back transformation (e.g. Fig. 1d), as seen in previous studies (Woodland et al. 2012; Myhill et al. 2016Woodland et al. 2023). At 30 GPa, the Mg-free sample (I1185-B) comprises a mixture of O6 and FeO (Fig. 1e). The phase coexisting with fper in the more Mg-rich sample (I1185-A) appears to be a product of back transformation (Fig. 1f), as discussed in the section on TEM results.

The nature of the Fe^{3+}-rich oxide coexisting with fper for experiments run at 1200 °C is shown in Fig. 3. At 6 and 10 GPa, spft coexists with fper over a wide range of $Fe^{2+}/(Fe^{2+}+Mg)$ ratios. At P > 10 GPa, fper coexists with the O5 phase, whose stability field is delimited at high $Fe^{2+}/(Fe^{2+}+Mg)$ ratios by the formation of the O6 phase and at lower ratios by the formation of periclase and hematite, as observed in the study of Uenver-Thiele et al. (2017b). The agreement with the study of Woodland et al. (2023) is very good except at 28 GPa, where their observation of Fe_4O_5 is at odds with Fe_5O_6 being found in this study at 30 GPa. As shown by Woodland et al. (2023), the transition between the O5 phase + Fe_xO field and the O6 field has a positive *P*–*T* slope, therefore the difference between the two studies can be explained by differences in *T*, as at these high-pressure conditions the *T* uncertainties may be of the order of 100 °C. The grey dashed line in Fig. 3 indicates compositions of spft and O6 oxides in equilibrium with fper with an $Fe_{tot}/(Mg+Fe_{tot})$ between 0.1–0.2, showing that with increasing pressure more Fe^{2+} is partitioning into the high-P Fe^{3+}-rich oxide phases. This change in partitioning can be described using an apparent Fe–Mg exchange coefficient:

$$K_D\,(\mathrm{app}) = \left(\left[Fe^{2+} + Fe^{3+}\right]/Mg\right)_{\mathrm{fper}} / \left(Fe^{2+}/Mg\right)_{\mathrm{oxide}} \quad (1)$$

which is defined using the total iron content of fper i.e. the apparent iron content determined by EMPA, but using the Fe^{2+} content of coexisting Fe^{3+}-rich oxides, which can be determined through stoichiometry.

TEM analyses

TEM lamellae were prepared from five samples: S7029, Z2151-B, Z2115-B and I1185-A and I1185-B. Fper in samples synthesized at 6 and 20 GPa show a mottled appearance in bright field (BF) images, indicating the presence of nano-sized (n-spft) exsolutions. High resolution imaging of sample S7029 (Fig. 4a) from 6 GPa indicates an average n-spft grain size of 10–12 nm. Moreover, the electron diffraction pattern (inset in Fig. 4a) can be indexed with fper and n-spft unit cell parameters (*a*) that are in a topotaxial relationship with $a_{fper} \cong \frac{1}{2}a_{n-spft}$. The samples from 20 GPa, composition A for sample Z2151-B and B for sample

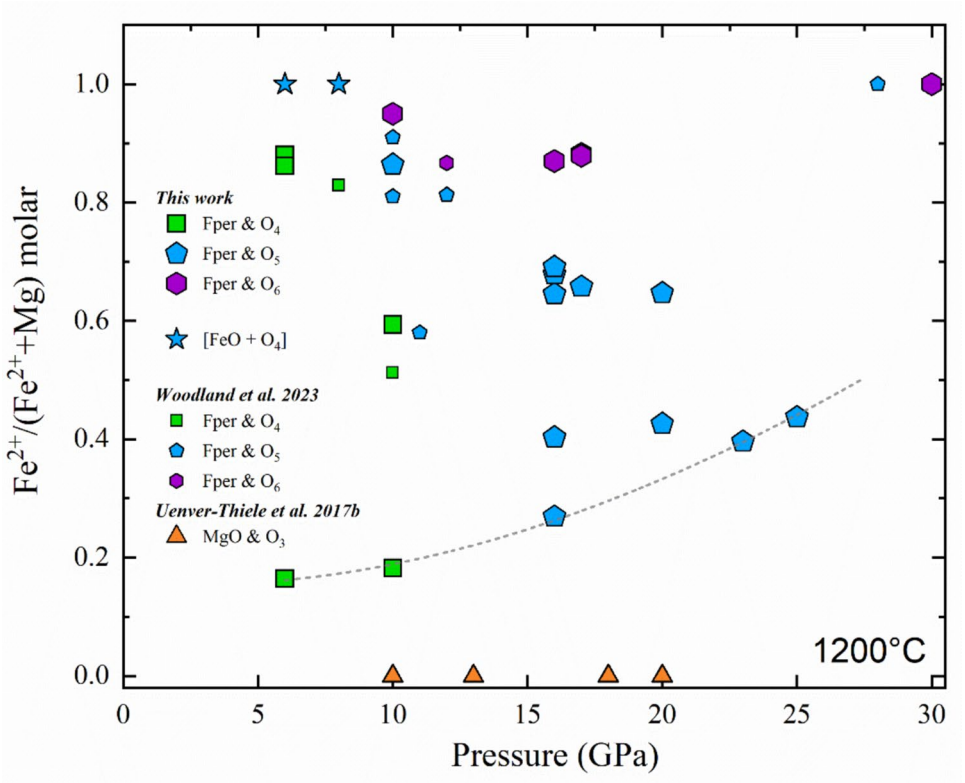


Fig. 3 The $Fe^{2+}/(Fe^{2+}+Mg)$ ratio of Fe^{3+}-rich oxides coexisting with fper in experiments run at 1200 °C. Larger symbols are from this study and smaller from Woodland et al. (2023) and Uenver-Thiele et al. (2017b). O4 indicates $(Fe^{2+},Mg)Fe_2^{3+}O_4$; O5 indicates $(Fe^{2+},Mg)_2Fe_2^{3+}O_5$, and O6 indicates $(Fe^{2+},Mg)_3Fe_2^{3+}O_6$. [FeO + O4] indicates experiments conducted with the Mg-free starting material where a higher-pressure phase appears to have back transformed to an assemblage of wüstite and magnetite during quenching, likely O5. MgO&O3 denotes experiments where Uenver-Thiele et al., (2017b) found an assemblage of periclase and hematite. The dashed grey line marks compositions in equilibrium with fper with a near constant $Mg/(Mg+Fe_{tot})$ ratio of ~0.85

Z2115-B, both have n-spft grain sizes of 1–5 nm (Fig. 4b). Furthermore, although both samples were produced at pressures above the breakdown of spft, the exsolution is still of n-spft in topotaxial relationship with the surrounding fper (inset in Fig. 4b). The fper grains of the Mg-free sample synthesized at 30 GPa (I1185-B) also show very weak diffraction spots that can be indexed as a topotaxial n-spft exsolution (Fig. 4c). The more Mg-rich sample synthesized at 30 GPa (I1185-A) contains fper grains with a markedly different type of exsolution, however, coexisting with an assemblage likely formed through back transformation of a high pressure Fe^{3+}-rich oxide. In the BF image (Fig. 4d) fper crystals can be seen to contain large exsolution lamellae in different orientations. However, the electron diffraction pattern of the fper grains, shown in the inset of Fig. 4d, can be indexed exclusively to the fper rock-salt structure, which indicates that either the lamellae grew incoherently with respect to fper, in spite of their regular pattern, or they may have become amorphous, during P or T quenching. Unfortunately, it was not possible to find a lamella with a suitable orientation for electron diffraction, but the change in the nature of the exsolution compared to the other samples, most likely indicates that it is not a spinel phase. The coexisting back transformed assemblage consists of at least two and probably three phases. It is possible to recognise some fper grains in this assemblage, referred to as [fper] in Fig. 4d, but these grains contain no exsolution lamellae and have a lower iron content (~6 wt % Fe) compared to the fper grains that host the large lamellae (~10 wt % Fe). The thickness of the sample unfortunately did not allow for an accurate analysis of the other phases in this back transformed assemblage. EMPA analyses indicate that the phase may have had an O4 composition (Table S1).

Ferropericlase Fe^{3+}/Fe_{total} ratios

Fper Fe^{3+}/Fe_{total} ratios were determined using Mössbauer spectroscopy (MS) and, for TEM-selected samples, by EELS. MS interpretation is complicated by overlapping peaks due to the presence of multiple Fe-bearing phases and by n-spft exsolution that forms in fper during quenching. Although some spectra can be deconvolved, MS uncertainties are large, so EELS was also employed. Samples from 30 GPa were too small for MS and were analysed only by EELS.

SEM images of a number of experiments performed below 12 GPa show that they contained only fper and Fe-Pt alloy. All but two of the MS collected for these samples contain magnetic sextets (Fig. 5a) originating from n-spft exsolution, however. The magnetic n-spft contribution to the spectra was fitted following the procedure described by Melai et al., (2026) and the results are reported in Table S3. To obtain the initial Fe^{3+} content in fper before exsolution, i.e. at the P–T synthesis conditions, the fper Fe^{3+}/Fe_{tot} ratio needs to be corrected to account for the contribution from

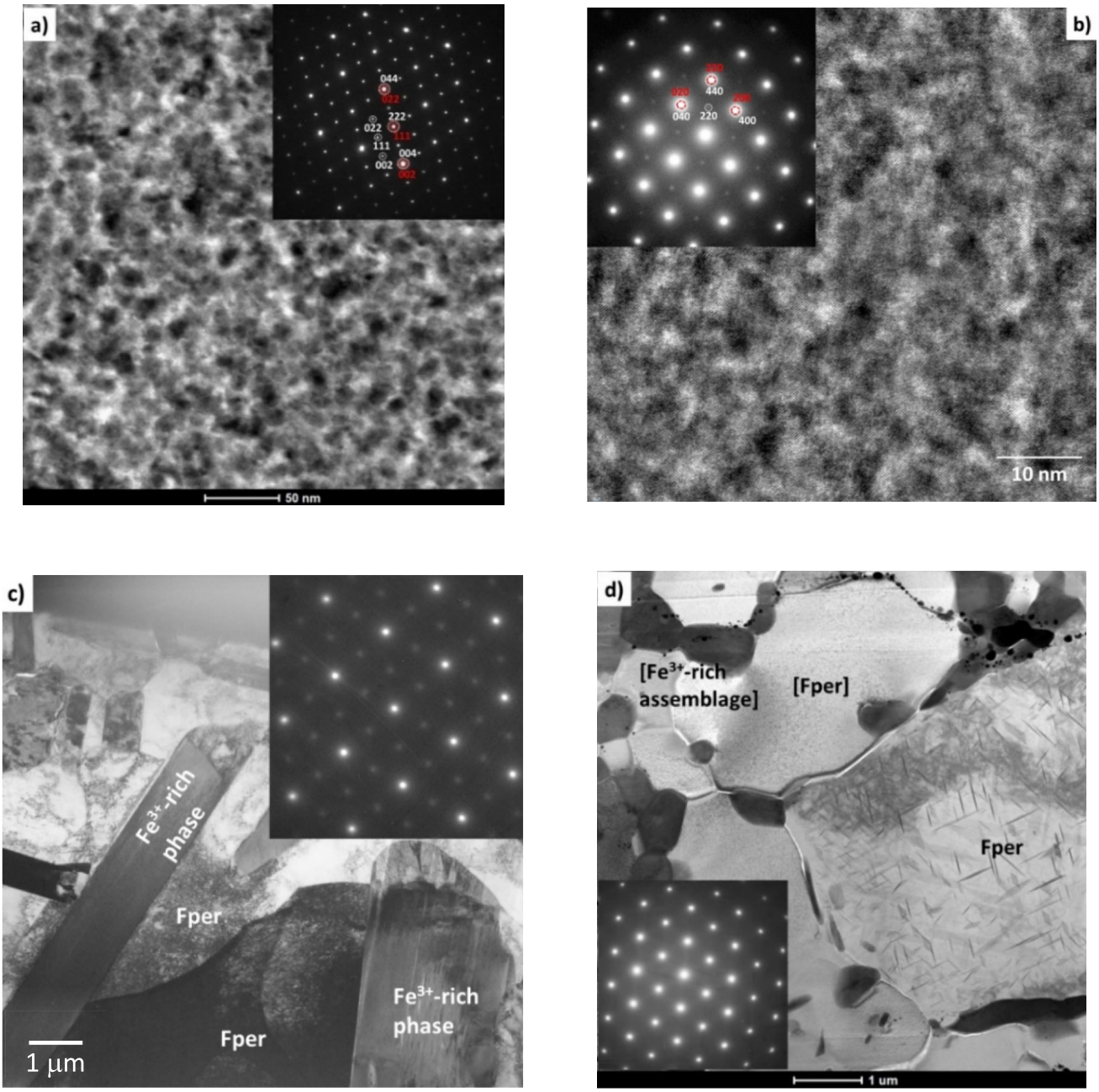


Fig. 4 High-resolution TEM images of fper grains from **a** sample S7029 recovered from 6 GPa and **b** sample Z2115-B recovered from 20 GPa with corresponding selected area electron diffraction (SAED) patterns (inset). Both fper grains show the presence of nm-sized exsolutions. The SAED contains reciprocal lattices of fper (red) and of an exsolved phase (white), which can be indexed to the spinel structure (n-spft). Note that the grain size of the exsolution in Z2115-B is smaller (~5 nm) than in S7029 (~10 nm). **c** Bright field TEM image of the Mg-free sample I1185-B from 30 GPa and SAED taken from one of the fper grains. The coexisting Fe^{3+}-rich phase is Fe_5O_6. The crystal orientation is the same as that of the fper grain in (**a**). Weak n-spft diffraction spots are visible in the SAED pattern (inset). **d** Bright field TEM image of sample I1185-A (also at 30 GPa) and the SAED (inset) taken from the fper grain containing the large lamellae, which indicates no additional diffraction spots in the SAED patterns except for fper. The Fe^{3+}-rich assemblage is most-likely a back transformation of a high-pressure unquenchable O4 phase-based on EMPA analyses

n-spft. To do this, the valence state of the fitted sextets is also considered. Where only an Fe^{3+} component was observed in the spectrum of the n-spft, its intensity was simply summed to that of the ferric iron of fper. In cases where the centre shift (CS) indicated the presence of an $Fe^{2.5+}$ component (Table S3), half of the intensity was taken for calculating the original fper Fe^{3+} content. Corrected and uncorrected fper Fe^{3+}/Fe_{tot} ratios are reported in Table 3, while the fitted

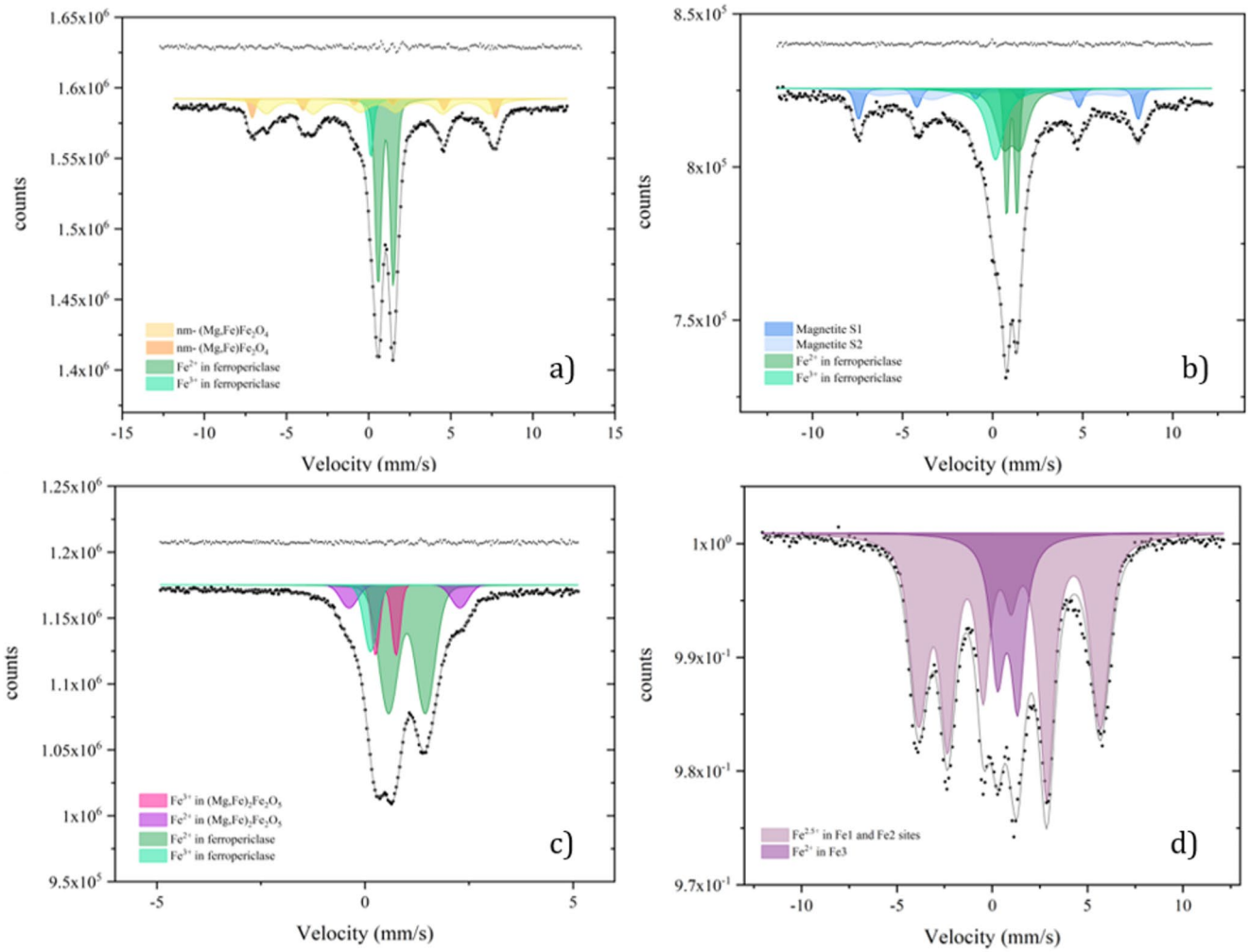


Fig. 5 Selected room-temperature fitted Mössbauer spectra. **a** Fper (S7509-B) is fitted with a doublet corresponding to Fe^{2+} (green) and a singlet for Fe^{3+} (light green), together with a broad magnetic sextet composed of two contributions arising from n-spft exsolution. **b** A well-defined sextet is fitted with two contributions S1 and S2 (blue and light blue, respectively) which can be assigned to the coexisting spft phase for sample S7029. **c** Two doublets belonging to the O5 phase coexisting with fper in sample Z2115-B are shown. **d** Mössbauer spectrum of the O6 phase in the monomineralic sample Z2120-A. In this spectrum a magnetic octet component (pink) is fitted to account for $Fe^{2.5+}$ in the octahedral sites, whereas the purple doublet is Fe^{2+} in the trigonal prism of this oxide structure

MS hyperfine parameters are reported in Table S3. The two samples of fper, S7470 and H5164, synthesised at 6 GPa and 1200 °C that did not exsolve n-spft, have fper Fe^{3+}/Fe_{tot} ratios of 0.11 and 0.09, respectively. These ratios may mark the limit at which Fe^{3+} can be quenched into fper without causing n-spft exsolution, at least at these P–T conditions and quench rates.

N-spft exsolutions are present also in fper grains coexisting with the macroscopic spft O4 phase (Fig. 5a). For these samples, the n-spft component could not be resolved in the Mössbauer spectra because it is overshadowed by the intense signal of the spft phase (Fig. 5b). Samples synthesized at pressures above 12 GPa and containing the O5 phase have no MS magnetic component. For the O5 phase this is likely due to the presence of magnesium in the octahedral site, which interrupts the long-range magnetic ordering reported for the Fe_4O_5 end member (Ovsyannikov et al. 2018). The O5 phase was fitted with two quadrupole doublets (Fig. 5c) corresponding to Fe^{2+} and Fe^{3+} sites. The Fe^{3+} doublet partly overlaps with the fper Fe^{3+} singlet, resulting in large uncertainties in the fper Fe^{3+}/Fe_{tot} ratio, particularly for samples with significant O5 contents. TEM SAED patterns indicate that n-spft exsolution still occurs in fper grains coexisting with the O5 phase, however, the lack of a MS magnetic component probably results from the smaller n-spft grain sizes, < 5 nm, (Fig. 4b), in these higher-pressure samples (e.g. Z2115-B). For these small grain sizes there is a collapse in the magnetic ordering to a superparamagnetic state and the sextet contracts to a central doublet

Table 3 Ferropericlase Fe^{3+}/Fe_{tot} ratios determined with Mössbauer spectroscopy and EELS

Sample	Fe^{3+}-rich phase	Fe^{3+}/Fe_{tot} in Fp	Fe^{3+}/Fe_{tot} with n-spft	EELS values
S7029	Spft	0.34 (4)	Signal overlap	0.58 (6)
Z2038	n-spft	0.16 (5)	0.21 (8)	
H5128	n-spft	0.14 (5)	0.33 (8)	
S7004	n-spft	0.25 (6)	0.44 (11)	
S7377	Spft	0.26 (5)	Signal overlap	
S7180	n-spft	0.22 (6)	0.63 (8)	
S7204	n-spft	0.20 (5)	0.46 (9)	
Z1949-B	n-spft	0.17(5)	0.50 (8)	
S7382	O_5 phase	0.15 (4)		
S7006	O_5 phase	0.24 (5)		
S7016	O_5 phase	0.11 (5)		
Z2151-B	O_5 phase	0.12 (5)		0.27 (1)
Z2153-B	O_5 phase	0.14 (6)		
H4792	O_5 phase	0.23 (5)		
S7410	O_5 phase	0.09 (3)		
S7123-B	O_5 phase	0.13 (5)		
I1185-A	[O_4 + fper]			0.15 (3)
S7470	Only Fper	0.11 (2)		
H5164	Only Fper	0.09 (2)		
S7510	n-spft*	0.13 (2)		
S7509-B	n-spft	0.12 (4)	0.34 (9)	
S7716-B	n-spft	0.12 (3)	0.41(8)	
Z2116	n-spft	0.15 (5)	0.40 (10)	
S7691-A	n-spft	0.09 (3)	0.28(7)	
Z2155-B	n-spft	0.11 (3)	0.34 (8)	
Z2155 A	n-spft	0.11 (2)	0.21(8)	
S7216-B	n-spft	0.13 (2)	0.36 (8)	
S7216-A	n-spft	0.13 (2)	0.37 (8)	
Z1949-A	n-spft	0.10 (2)	0.32 (8)	
Z2122-B	O_5 phase	0.13 (5)		
Z2117-B	O_5 phase	0.13 (5)		
Z2115-B	O_5 phase	0.15 (5)		0.16 (2)
Z2121-A	O_5 phase	0.18 (6)		
Z2151-A	O_5 phase	0.15 (5)		
Z2153-A	Only Fper	0.25 (2)		
H5189-A	n-spft	0.14 (3)	0.38 (10)	
S7495-A	Spft	0.12 (3)	Signal overlap	
H5190-A	O_5 phase	0.14 (6)		
Z2077-A	O_5 phase	0.19 (5)		
H5189-B	Spft	0.13 (4)	Signal overlap	
S7509-A	Spft	0.11 (4)	Signal overlap	
S7604-A	Spft	0.08 (5)	Signal overlap	
S7716 A	Spft	0.05 (3)	Signal overlap	
S7691-B	Spft	0.07(3)	Signal overlap	
I1185- B	O_6 phase			0.03 (1)

*A very small magnetic n-spft signal is visible in the MS, but it cannot be fitted. [O_4 + fper] indicates a back-transformed assemblage

(Hartridge et al. 1997; Goya et al. 2003; Castellanos-Rubio et al. 2019).

In several experiments using the nominal ($Mg_{0.05}Fe_{0.95}$)O composition (D) with no added Fe_2O_3, only the O6 phase was synthesised, indicating that the multianvil assembly is intrinsically oxidising. The MS for the O6 phase is shown in Fig. 5d from sample Z2120-A. The Mössbauer spectrum consists of two components: a magnetic octet corresponding to $Fe^{2.5+}$ at the Fe1 and Fe2 octahedral sites (CS = 0.65 mm/s), and a doublet corresponding to Fe^{2+} in the Fe3 trigonal prism (CS = 0.88 mm/s) (Table S3) of the Fe_5O_6 structure (Lavina and Meng 2015; Ovsyannikov et al.2018). In this case the presence of < 3 wt. % Mg is not sufficient to alter the magnetic ordering.

EELS measurements have the advantage that they can be performed on individual grains in the samples and they provide an average Fe^{3+}/Fe_{tot} ratio that includes the n-spft exsolution and is representative of the fper ratio at the synthesis conditions. The EELS spectra collected for fper grains from all five samples analysed at the TEM are shown in Fig. S2. As pressure increases, the L_3 edge maximum moves toward lower energies, which is a qualitative indication that the fper Fe^{3+}/Fe_{tot} ratio is decreasing. The spectra have been fitted and analysed following the procedure outlined in Melai et al., (2026). The resulting Fe^{3+}/Fe_{tot} ratios are reported in Table 3.

Thermodynamic modelling

To extract information on the formation conditions of fper inclusions in diamonds, a thermodynamic model was developed that calculates the Fe^{3+}/Fe_{tot} ratio of fper as a function of P, T, MgO content and fO_2. To do this, P-dependent thermodynamic terms were fitted using the high P experimental dataset to extend the room pressure thermodynamic model presented in Melai et al., (2026).

The fO_2 of each experiment is calculated using the composition of the Pt-Fe alloy and the equilibrium:

$$2Fe_{(alloy)} + O_2 \leftrightarrow 2\ FeO_{(fper)} \quad (2)$$

Although the experiments also contain Ni, its concentration is < 1 wt. % in the alloy, which is, therefore, assumed to be a Pt-Fe binary, with activity composition relations from Kessel et al. (2001) and P-dependences refined in the model.

The fper $\Delta_m G^{ex}$ is described with the subregular expression from Jung et al. (2004),

$$\begin{aligned}\Delta_m G^{ex} = {} & X_{FeO}X_{FeO_{1.5}}q^{00}_{FeO,FeO_{1.5}} + X_{FeO}X_{FeO_{1.5}}\left(1 - X_{FeO_{1.5}}\right)q^{10}_{FeO,FeO_{1.5}} \\ & + X_{FeO}X_{MgO}q^{00}_{FeO,MgO} + \left(X_{FeO_{1.5}}\right)^2 X_{MgO}q^{10}_{FeO_{1.5},MgO} \\ & + X_{MgO}X_{FeO_{1.5}}\left(1 - X_{FeO_{1.5}}\right)^2 q^{02}_{FeO_{1.5},MgO}\end{aligned} \quad (3)$$

where the five non-ideal interaction parameters, q, have P-dependent terms fitted to the experimental data. The activity coefficients are then calculated in the same way as described below for FeO:

$$RT\ln\gamma_{\mathrm{FeO}}^{\mathrm{Fper}} = \Delta_{\mathrm{m}}G^{\mathrm{ex}} - X_{\mathrm{FeO_{1.5}}}\left(\frac{\partial\Delta_{\mathrm{m}}G^{\mathrm{ex}}}{\partial X_{\mathrm{FeO_{1.5}}}}\right)_{\mathrm{MgO}} - X_{\mathrm{MgO}}\left(\frac{\partial\Delta_{\mathrm{m}}G^{\mathrm{ex}}}{\partial X_{\mathrm{MgO}}}\right)_{\mathrm{FeO_{1.5}}} \quad (4)$$

P-dependencies of spft interaction parameters were also refined. Standard state Gibbs free energies of formation were taken from previous thermodynamic refinements (Holland and Powell 2011; Hidayat et al. 2015; Myhill et al. 2016). Equation of state dependencies for MgO, FeO and Fe (Tange et al. 2009; Campbell et al. 2009; Dorogokupets et al. 2017) were fitted to the equations used in the Holland and Powell (2011) database. The room P and T volume (V_0) and thermal expansion of the fper $FeO_{1.5}$ end-member were allowed to vary in the refinement.

The model was refined using the experimental data on the composition of fper coexisting with spft up to 10 GPa by refining P-dependent terms until model differences with experimental values of fper-spft K_D(app), fper Fe^{3+} and log fO_2 were minimized. The coexisting compositions are determined by the model at spft saturation using the equilibria:

$$\mathrm{MgFe_2O_{4(spft)}} + \mathrm{FeO_{(fper)}} \leftrightarrow \mathrm{Fe_3O_{4(spft)}} + \mathrm{MgO_{(fper)}}, \quad (5)$$

and

$$\mathrm{FeO_{(fper)}} + \mathrm{2FeO_{1.5(fper)}} \leftrightarrow \mathrm{Fe_3O_{4(spft)}}, \quad (6)$$

In this way the fO_2 is also constrained independently in the model by the equilibria:

$$\mathrm{4FeO_{(fper)}} + \mathrm{O_2} \leftrightarrow \mathrm{4FeO_{1.5(fper)}} \quad (7)$$

and

$$\mathrm{3FeO_{(fper)}} + \mathrm{0.5O_2} \leftrightarrow \mathrm{Fe_3O_{4(spft)}} \quad (8)$$

and can be evaluated against the results obtained using equilibrium (2). Experiments containing only fper and Pt-Fe alloy were also used in the refinement by modelling the experimental fper composition using Eqs. (2) and (7). The thermodynamic properties of spft end-members are very well established and for the magnesioferrite end-member are well constrained by the breakdown reaction to $MgO + Fe_2O_3$ determined by Uenver-Thiele et al. (2017b) between 8 and 10 GPa. Further constraints were included in the refinement by calculating coexisting fper and O5 phase compositions using equilibria analogous to (5) and (6), and comparing the results with the experimental data. End-member properties for Fe_4O_5 were constrained from the phase relations of the reaction $4Fe_3O_4 = 2Fe_4O_5 + 2Fe_2O_3$ (Woodland et al. 2012) and for the $Mg_2Fe_2O_4$ endmember from the reaction $2MgO + Fe_2O_3 = Mg_2Fe_2O_4$ (Uenver-Thiele et al. 2017a, b). To obtain a better fit to the experimental Fe –Mg partitioning data, the Fe_3O_4 stability field had to be shifted to the upper limit of its pressure-uncertainty range. Including the O5 phase in the model also allows an independent assessment of the experimental fO_2 to be obtained from the equilibrium:

$$\mathrm{4FeO_{(fper)}} + \mathrm{0.5O_2} \leftrightarrow \mathrm{Fe_4O_{5(O5)}} \quad (9)$$

which is independent of the iron activities in the Fe-Pt alloy. No improvement in the model fit was obtained by including non-ideal Fe–Mg mixing terms for the O5 phase. The O6 phase was not included in the fitting because its stability field is limited, and it would not provide further useful constraints.

All standard state data and mixing terms are reported in Tables S4 and S5. Only three of the five fper interaction parameters required P-dependent terms. Of these $q^{00}{}_{\mathrm{FeO\text{-}MgO}}$ was fixed at the value determined by Frost (2003). There is some trade-off between the P-dependence of the fper interaction parameters and the V_0 of the fper $FeO_{1.5}$ component, however, the refinement that fitted the observations with the smallest interaction parameter P-dependences was favoured. In the final optimisation, the independently calculated fO_2 values for experiments where fper coexists with spft or O5 generally agreed within < 0.5 log units, although some clear outliers remain. A spreadsheet with different types of model calculations is provided as a supplementary file.

Figure 6a shows calculations using the resulting thermodynamic model for the fO_2 at which fper is in equilibrium with spft at 6 GPa and the O5 phase at higher pressures. The model is compared with the experimental fO_2, determined with the Fe-Pt sliding redox sensor. Although the experiments at 30 GPa did not contain the O5 phase, the data of Woodland et al. (2023) indicate that the O5 stability field is relatively close to these experimental conditions. As can be seen in Fig. 6b, the model is able to consistently reproduce the Fe^{3+}/Fe_{tot} ratio of fper coexisting with either spft or the O5 phase between room pressure and 30 GPa. MS measurements at 6 GPa have large uncertainties due to overlaps between sextets originating from both n-spft exsolution and coexisting spft, hence the importance of the EELS measurements shown by stars in Fig. 6b. At higher pressures, however, the fper MS signal can be well resolved from the O5 pattern (Fig. 5c) and there is good agreement with the model

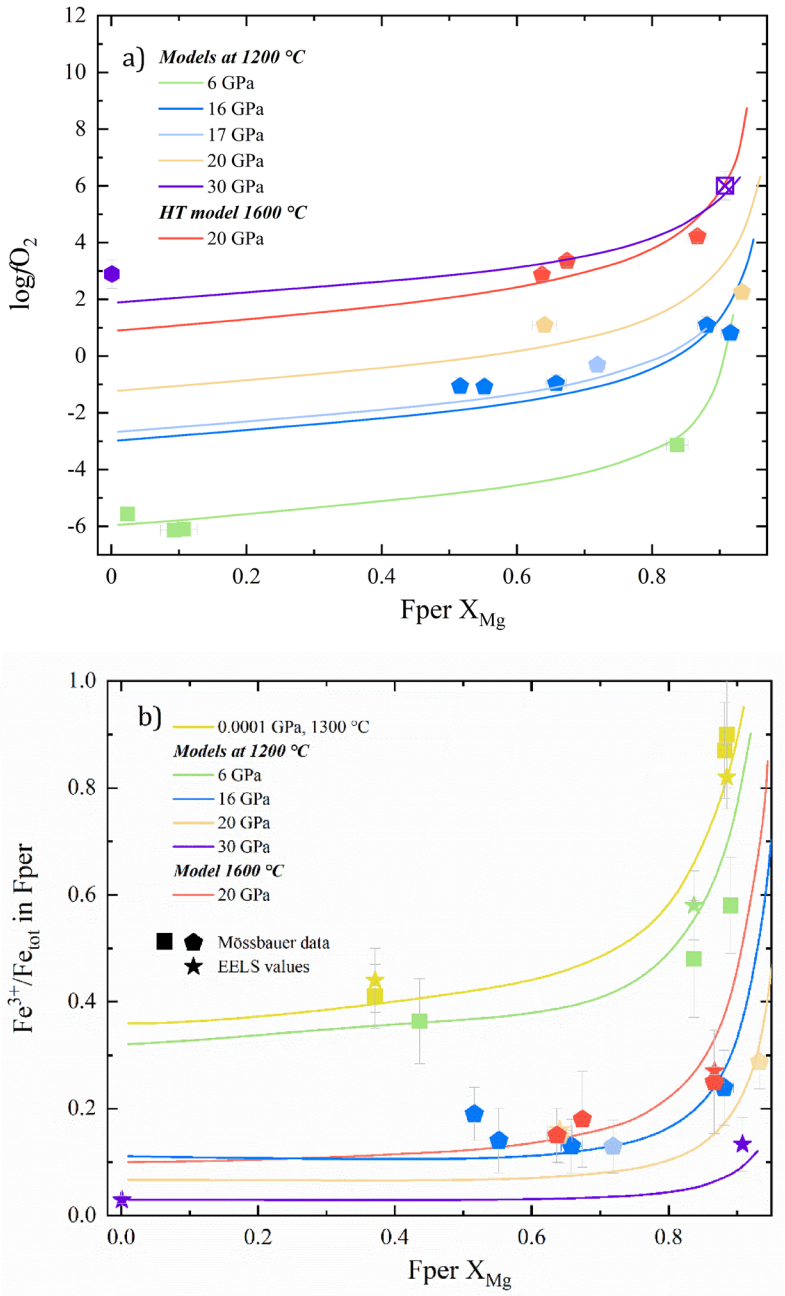


Fig. 6 **a** The fO_2 determined using the Fe–Pt alloy redox sensor for experiments where fper coexisted with spft (6 GPa; square symbols) and the O5 phase (16–20 GPa; pentagons). Solid curves are calculated for the same equilibria using the thermodynamic model. At 30 GPa the coexisting phases are O6 (hexagon) and an unquenchable phase (square with cross), but the model assumes the O5 phase is present. **b** The measured Fe^{3+}/Fe_{tot} ratios of fper coexisting with Fe^{3+}-rich oxides. The same symbols are used as in **a**. Data are compared with the calculations from the thermodynamic model

(Fig. 6b), except in a few instances where the proportion of the O5 phase in the sample is relatively high. The overall agreement between the measured fper Fe^{3+}/Fe_{tot} ratios and the thermodynamic model can be assessed in Figs. S3a and Figs. S3b for experiments performed at pressures below and above 10 GPa respectively. A number of the experiments from below 10 GPa were performed at fO_2 conditions lower than the spft field, where MS contain only signals from fper or from fper and exsolved n-spft. These samples are all in very good agreement with the model, whereas samples that also coexisted with macroscopic spft show a larger deviation. Similarly, in Fig. S3b the three samples that show a greater deviation from the model contained a relatively large proportion of the O5 phase. Values for the iron-wüstite (IW) buffer calculated with the model are consistent with the re-evaluation of Hirschmann (2021), lying within 0.2 log units at 30 GPa and 1300 °C and within 0.3 log units at 2000 °C.

Figure 7 shows experimental values of the fper-spft and fper-O5 K_D(app), as defined by Eq. (1), describing the Fe–Mg partitioning between the coexisting oxides. The model is in reasonable agreement with the experimental values over the entire pressure and temperature range. The K_D(app) uses the total Fe content of fper as measured by EPMA, so the model must reproduce the fper Fe^{3+}/Fe_{tot} ratio in order

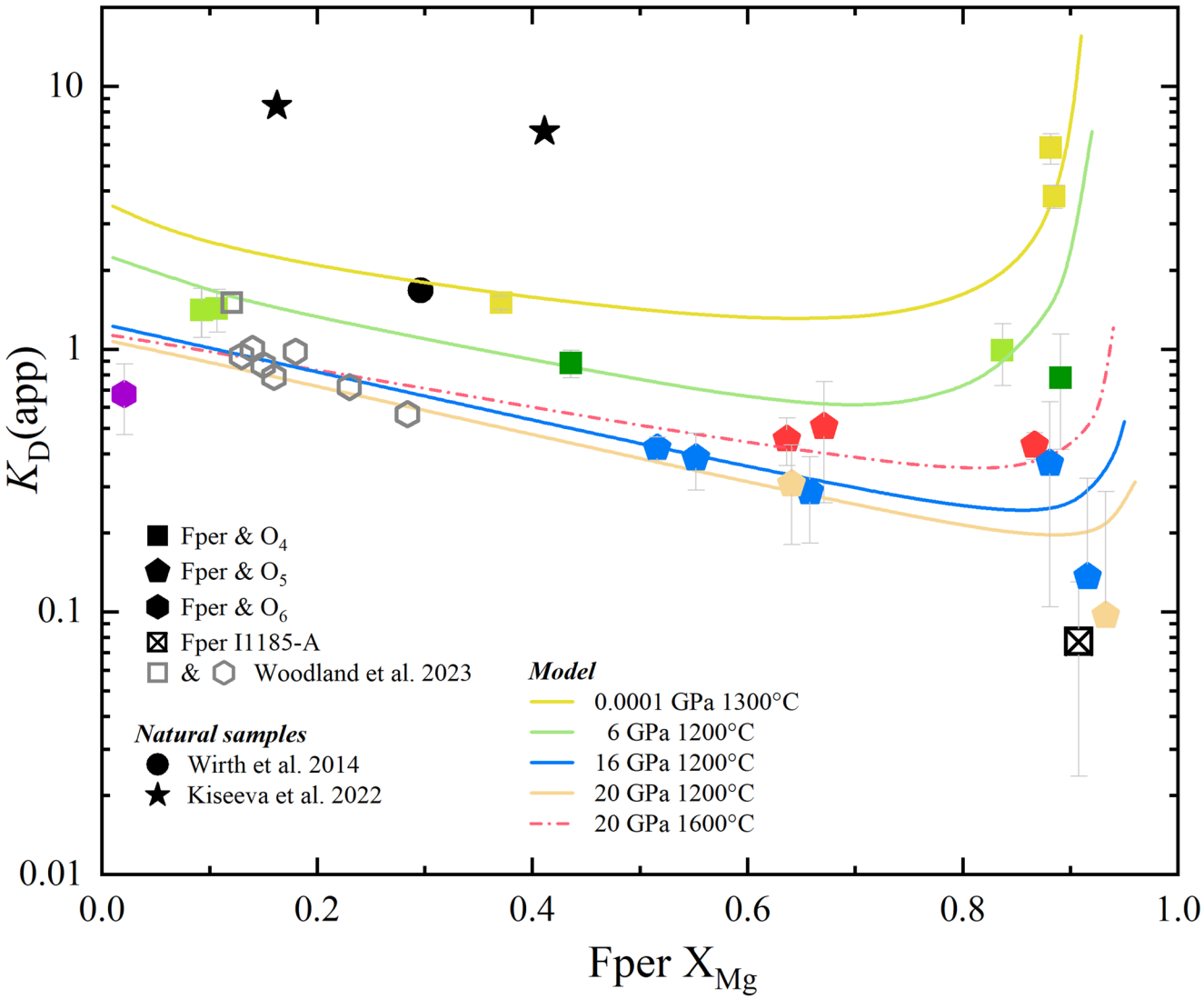


Fig. 7 The apparent Fe–Mg distribution coefficient K_D(app), as defined in Eq. (1), for fper Fe–Mg exchange with coexisting Fe^{3+}-rich oxides. The data are from the conditions indicated by the colour coding of the thermodynamic model calculations (solid and dashed lines). Data at 10 GPa are indicated by darker green squares but the model is not shown as it is very close to the 6 GPa curve. Conditions from Woodland et al. (2023) are 8 GPa, 1200 °C for O4 and 10–20 GPa, 1100–1500 °C for O6. The circle and stars indicate analyses from fper inclusions in natural diamonds showing spft exsolution, from Wirth et al. (2014) and Kiseeva et al. (2022), respectively. Fper in sample I1185-A from 30 GPa coexists with a back transformed phase that has the composition of an O4 phase

to predict the correct value. This makes K_D(app) sensitive to the fper Fe^{3+}/Fe_{tot} ratio but not dependent on the uncertainties involved in its measurement. K_D(app) decreases with increasing pressure, which means the coexisting Fe^{3+}-rich oxide becomes more Fe^{2+}-rich, as indicated by the dashed curve in Fig. 3 for fper with X_{Mg} between 0.8–0.9.

Although some mismatch remains, the fO_2, Fe^{3+}/Fe_{tot}, and K_D(app) datasets provide independent constraints on the P-dependent thermodynamic properties and the model is therefore well optimised. In the refinement the P-dependences of the Fe-Pt Margules parameters were also allowed to vary. However, satisfactory solutions were only found when these pressure dependences were at or near zero. Recently Hirschmann and Zhang (2023) re-examined iron activities in the Fe-Pt system and proposed a slightly different set of Margules parameters to those used here (Kessel et al. 2001) and proposed values for the pressure dependencies of the Fe−Pt Margules parameters of W^{V}_{FePt} = 0.107 kJ/mol/kbar and W^{V}_{PtFe} = 0.166 kJ/mol/kbar. Using these to calculate fO_2 leads to differences that increase with MgO content and pressure. At 30 GPa, the calculated fO_2 is 1.3 log units lower for the FeO end-member sample (I1185-A) and 2.5 log units lower for the MgO-rich sample (I1185-B). However, using these values makes it impossible to refine the model to match all fO_2 values from equilibria (2), (7),

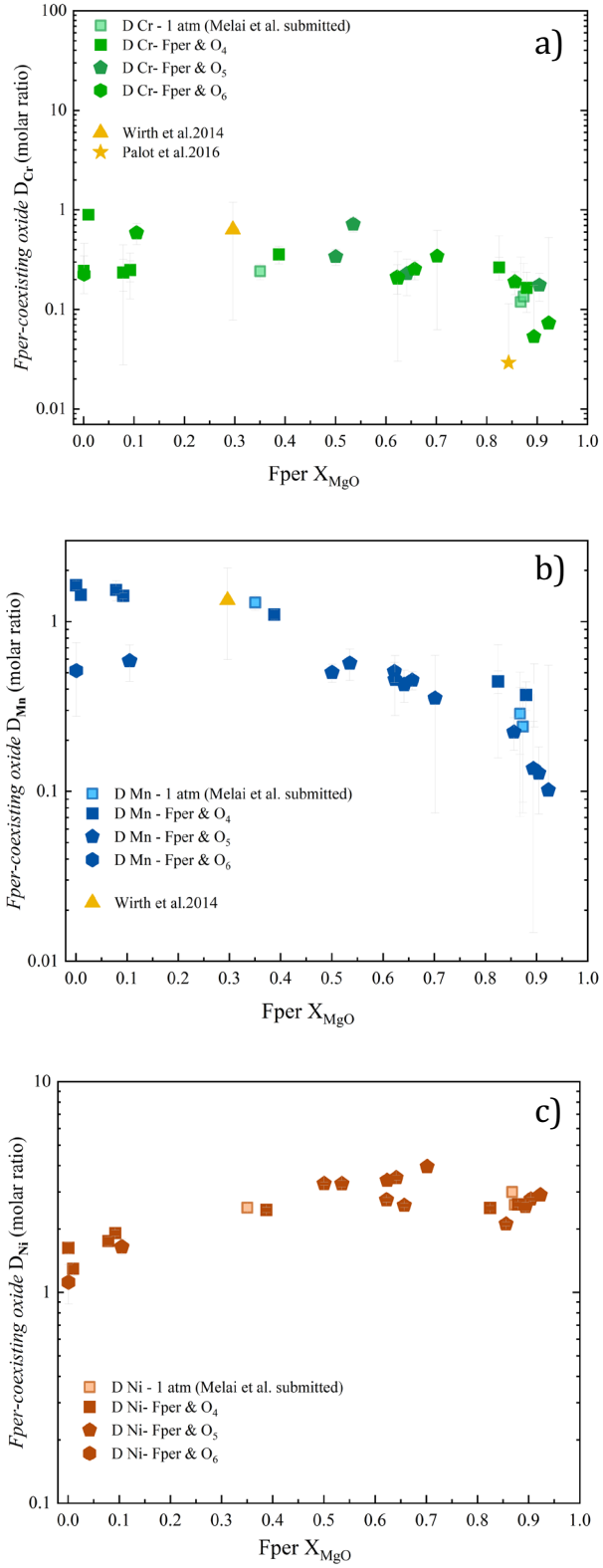


Fig. 8 The partition coefficient, *D*, of **a** Cr, **b** Mn and **c** Ni between fper and either spft, O5, O6 or [O4] phases. Symbols in yellow show natural samples where TEM measurements have allowed spft exsolutions within fper inclusions in diamonds to be analysed

(8), and (9), keeping in mind that equilibria (8) and (9) are independent of the Fe–Pt sensor. Although the pressure dependence of Fe–Pt Margules parameters is unlikely to be zero, this result indicates that they are smaller than implied by the 1-bar excess volume terms.

Partitioning of Cr, Mn and Ni between fper and high pressure Fe^{3+}-rich oxides

Figure 8 shows partition coefficients for three minor elements between fper and coexisting Fe^{3+}-bearing oxides. For partitioning involving any particular phase there does not appear to be a strong change with either *P* or *T*. Mn shows one of the clearest overall trends with the MgO content of fper, caused likely by an increase in Mn valence state with increasing MgO, which corresponds to increasing fO_2. The O5 and O6 phases show strong differences in partitioning for Mn at low Mg-contents. There appears to be some tendency for higher D_{Cr} values for the O5 phase and particularly for the [O4] phase resulting from the back transformation of the unquenchable high-pressure precursor present in sample I1185-A at 30 GPa. This [O4] phase also has higher D_{Ni} values and to a lesser extent D_{Mn}.

Discussion

Nano-spinel ferrite exsolution from ferropericlase

All samples examined using TEM, except sample I1185-A, show coherent, topotaxial exsolution of n-spft within the fper grains, which is also evident in XRD analyses (Fig. 2). These n-spft exsolutions occurred at pressures (20–30 GPa), well above the stability field (< 10 GPa) of the spinel ferrite phase (Uenver-Thiele et al. 2017a,b; Woodland et al.2023). Although the sample pressure may decrease during T quenching, this decrease is normally not more than a few GPa (Armstrong et al. 2020). It is more likely, therefore, that the formation of n-spft is controlled by topotaxy with the fper structure. At high P and T, Fe^{3+} is likely disordered on octahedral sites in fper, with locally ordered octahedral cation vacancies providing charge balance. Upon quenching Fe^{3+} atoms drop into interstitial tetrahedral positions coordinated with octahedral vacancies. These defects migrate to form larger clusters (Koch and Cohen 1969; Hazen and Jeanloz 1984; Dimitrov et al. 1999) to maintain charge neutrality and minimise strain energy. Their accumulation on further cooling, forms regions of coherent n-spft exsolution, as the oxygen sublattices of both phases are nearly identical in size.

On closer inspection, however, the unit cell parameters determined for n-spft range up to 8.456 Å (Table S2), which is significantly larger than the range reported for spft compositions, ~8.40 Å (Melai et al. 2023). This expansion of the n-spft unit cell can be rationalised, however, as it results in a better fit to the fper oxygen sublattice, thus minimising lattice strain across the grain boundaries. Conversely, there seems to be also evidence that the unit-cell parameters of fper contract upon n-spft exsolution, for the same reason (Melai et al. 2026). Fper unit cell parameters from our study and from Woodland et al., (2023), are much smaller than those reported for samples with negligible Fe^{3+} contents, for the same MgO content (Fig. S4), bearing in mind that the majority of these samples have quenched fper Fe^{3+}/Fe_{tot} ratios that are also relatively low, as most of the Fe^{3+} has exsolved into n-spft.

However, aside from a qualitative tendency for fper containing n-spft to have lower unit-cell parameters, there is no consistency among these lattice parameters that would allow them to be fit purely as a function of their MgO, FeO and Fe_2O_3 contents. A good explanation for this lack of reproducibility, is that the fper unit cell parameters are also influenced by lattice strain caused by differing proportions and grain sizes of n-spft exsolution. Ferropericlase samples synthesised at 5 GPa and 1300 °C by Dobson et al. (1998), for example, have very high Fe^{3+}/Fe_{tot} ratios (up to 0.7) but unit-cell parameters similar to nearly Fe^{3+}-free fper (Fig. S4), comparable to the Fe-saturated samples of O'Neill et al. (2003). Although the MS show no magnetic component to indicate n-spft exsolution, this may still have occurred with grain sizes small enough for the n-spft to be superparamagnetic, in which case the MS signal collapses into a Fe^{3+} doublet (Hartridge et al. 1997; Goya et al. 2003; Castellanos-Rubio et al. 2019; Melai et al. 2026).

If n-spft exsolution influences the fper unit-cell parameter, it could in principle have also affected other physical property measurements. As the coordination of Fe^{3+} in ferropericlase changes during quenching, in situ measurements would be required to determine the coordination at high temperatures and pressures.

The ferropericlase stability field and Fe^{3+}/Fe_{tot} ratio as a function of fO_2

In Figs. 9 and 10 the log fO_2 and Fe^{3+}/Fe_{tot} ratios that delimit the stability field of a typical lower mantle $(Mg_{0.8}Fe_{0.2})_XO$ fper composition, are calculated as a function of P at 1200 °C. In equilibrium with spft, the fper Fe^{3+}/Fe_{tot} ratio increases with pressure, but after the phase transformation to the O5 phase, it decreases sharply (Fig. 10). This is in qualitative agreement with previous studies that show fper Fe^{3+}/Fe_{tot} ratios extending to high values (i.e. > 0.5)

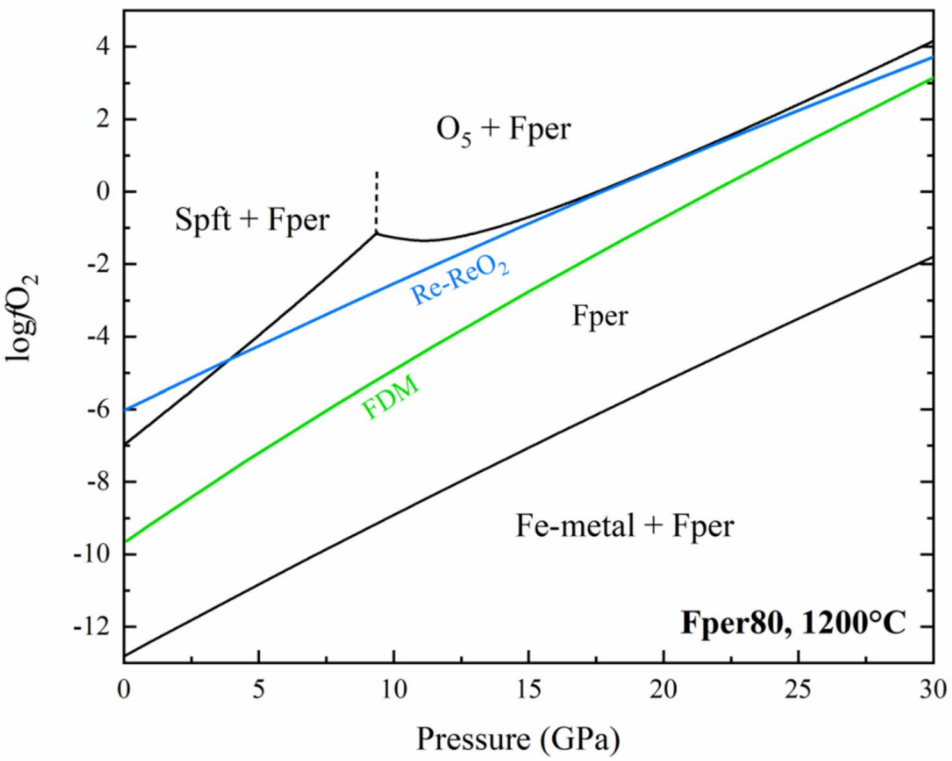


Fig. 9 The variation in log fO_2 with pressure at 1200 °C under conditions where $(Mg_{0.8}Fe_{0.2})_XO$ fper coexists with either spft or O5 or with iron metal, as indicated (solid black curves). Curves for the Re-ReO_2 oxygen buffer (blue) and the equilibrium between fper, diamond and magnesite, (FDM) are also shown (see text for details)

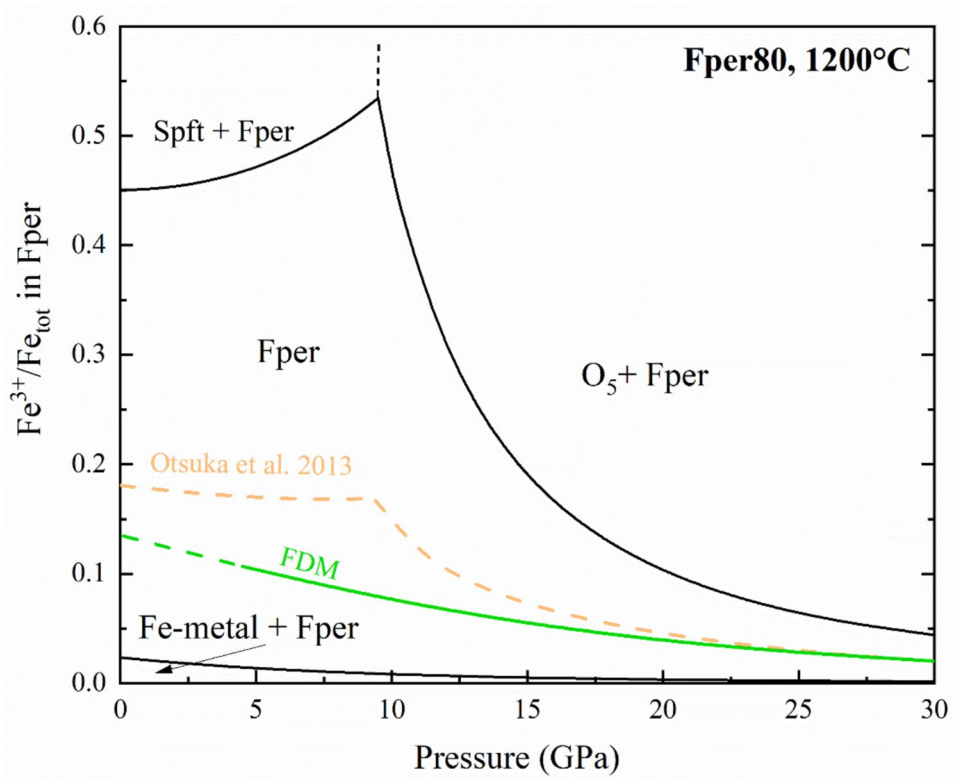


Fig. 10 The fper Fe^{3+}/Fe_{tot} ratio is plotted at conditions where $(Mg_{0.8}Fe_{0.2})_XO$ fper coexists at 1200 °C with either spft or the O5 phase or with iron metal (black curves), as in Fig. 9 and along the FDM (fper, diamond, magnesite) buffer (green curve). The yellow dashed line shows the results of the model of Otsuka et al. (2013) calculated along the fper-spft and fper-O5 fO_2 curves shown in Fig. 9

at 1 atmosphere (Brynestad and Flood 1958; Katsura and Kimura 1965; Speidel 1967; Melai et al. 2026) and at pressures up to 5 GPa (Dobson et al. 1998), but decreasing at pressures > 10 GPa (McCammon et al. 1998; Bolfan-Casanova et al. 2002; Otsuka et al. 2010). In detail, however, there are several inconsistences between our model and results from previous high P experimental studies.

Otsuka et al. (2010) performed MS measurements on recovered fper of approximately the same $(Mg_{0.8}Fe_{0.2})_XO$ composition. They report fper Fe^{3+}/Fe_{tot} ratios, from samples produced at 5 GPa, 1400–2000 °C and the Re–ReO_2 buffer, ranging from 0.2 to 0.14, whereas we calculate much higher ratios of 0.39 to 0.32 at the same conditions at the Re–ReO_2. Bolfan-Casanova et al. (2002) report Fe^{3+}/Fe_{tot} ratios for $(Mg_{0.93}Fe_{0.07})_XO$ fper also buffered at Re–ReO_2 and at 1200 °C, that decrease from 0.16 to 0.01 between 5 and 25 GPa, whereas we calculate a decrease from 0.37 to 0.05 over the same conditions at Re–ReO_2. These previously measured low values, particularly at 5 GPa, are inconsistent with the fact that the fO_2 of the Re–ReO_2 buffer is close to the upper limit in fper stability for these compositions (Fig. 9) and that much higher Fe^{3+}/Fe_{tot} ratios have been reported, not only in our study but in that of Dobson et al. (1998).

This underestimation of the fper Fe^{3+}/Fe_{tot} ratio might result from quenched n-spft exsolution that went unnoticed in MS measurements, due to the collected velocity range being too narrow. However, a further issue is that both studies used large single crystals of fper, with dimensions of ~ 0.5 mm, as starting materials that were surrounded by buffering materials. In order to reach equilibrium, solid state diffusion over large distances within the crystal would have been required, and such an assemblage is probably not effective at buffering the entire sample, particularly given that large amounts of fper oxidation would be needed to reach Re–ReO_2 equilibrium.

The analyses of these likely ineffectively buffered Re–ReO_2 fper samples were used to calibrate the model of Otsuka et al. (2013) for predicting the ferric iron content of fper as a function of composition, P, T and fO_2. As can be seen in Fig. 10, this model significantly underestimates the ferric iron content of fper when it is employed at fO_2 conditions along the fper-spft and fper-O5 boundaries. Although the difference between the two models improves towards lower fO_2, there is a tendency for the Otsuka et al. (2013) model to overestimate the fO_2 calculated for a particular fper Fe^{3+}/Fe_{tot} ratio. Kaminsky et al. (2015), for example, used the equation of Otsuka et al. (2013) to calculate the fO_2 of fper inclusions in diamonds assuming conditions at the top of the lower mantle (25 GPa, 1687 °C), and obtained fO_2 values between + 1 log unit and + 8 log units above the iron-wüstite (IW) buffer. Using our thermodynamic model,

the inclusions fall in the range +2 to +5 log units above IW at the same conditions.

The conditions of fper inclusion formation in diamonds

Fe^{3+}/Fe_{tot} ratios of fper inclusions in diamonds reach values up to ~ 0.14 (McCammon et al. 2004; Otsuka et al. 2013; Wirth et al. 2014; Kaminsky et al. 2015; Nestola et al. 2016). At 1200 °C our model predicts the maximum Fe^{3+}/Fe_{tot} ratio for $(Mg_{0.8}Fe_{0.2})_XO$ fper at the top of the lower mantle to be only 0.05 (Fig. 10), but at adiabatic temperatures (~ 1900 °C) it can reach ~ 0.2, before the O5 phase would replace fper. Thus, based on O5 phase stability alone, there is no reason to suspect that these inclusions could not have formed at least at the top of the lower mantle.

However, as the fper inclusions would be in equilibrium with diamond, then the reaction:

$$MgO_{(per)} + C_{(diamond)} + O_2 \leftrightarrow MgCO_{3(magnesite)} \quad (10)$$

provides a more realistic limit to the fO_2, and thus the fper Fe^{3+}/Fe_{tot} ratio. Above equilibrium (10), diamond and fper react to magnesite, and melting of magnesite would still impose an fO_2 below FDM (Stagno and Frost 2010). Most other components (e.g., Ca) stabilise the carbonate side of the reaction and therefore lower the effective fO_2 limit. Fe has the opposite effect because it partitions more strongly into fper, which can be accounted for by the parallel equilibrium,

$$FeO_{(fper)} + C_{(diamond)} + O_2 \leftrightarrow FeCO_{3(siderite)} \quad (11)$$

Using a van Laar model for FeMg interaction in the single-site disordered carbonate (Kang et al. 2016) and the standard state data given in Table S4, the fO_2 of this fper–diamond–(Fe-bearing) magnesite buffer (FDM) and the composition of the coexisting carbonate can be calculated by solving Gibbs free energy expressions for Eqs. (10) and (11) simultaneously. Figure 11 shows the resulting carbonate-fper Fe–Mg distribution coefficient ($K_D = [Fe^{2+}/Mg]_{Carb}/[Fe^{2+}/Mg]_{Fper}$) calculated at 1600 °C and different pressures. The calculation reproduces very well data from Stagno et al. (2011) at 25 and 45 GPa and Bulatov et al. (2019) from 7.5 and 10.6 GPa. Carbonates from the study of Bulatov et al. (2019) also contained Ca, which explains the higher K_D values but, as stated previously, this would lead to a lowering of the FDM fO_2.

Using the thermodynamic model, the fper Fe^{3+}/Fe_{tot} ratio at the FDM buffer is calculated in Fig. 12, at P–T conditions that follow an adiabatic gradient (Katsura 2022), except at 25 GPa, where two temperatures are chosen (1200 °C and

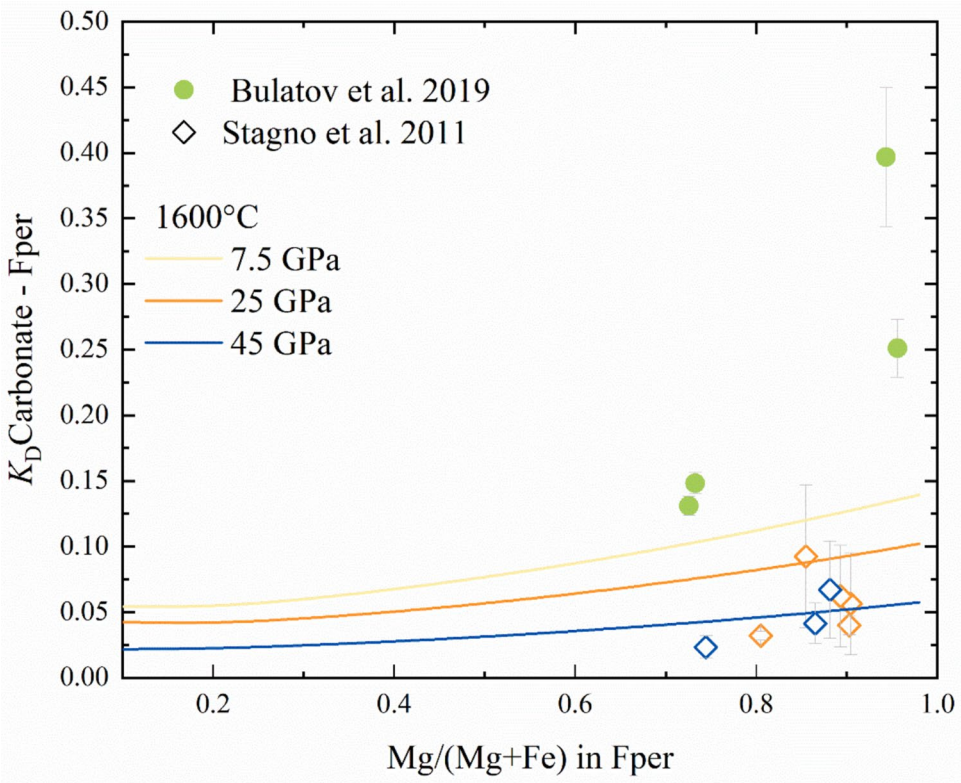


Fig. 11 The carbonate-fper Fe–Mg distribution coefficient, K_D, as a function of the fper Mg/(Mg + Fe) ratio is calculated at 1600 °C and different pressures. Stagno et al. (2011) data are from 25 and 45 GPa and 1500–1700 °C, while data from Bulatov et al. (2019) are from 7.5 and 10.5 GPa and 1550–1600 °C. In the latter study, the carbonates also contain Ca

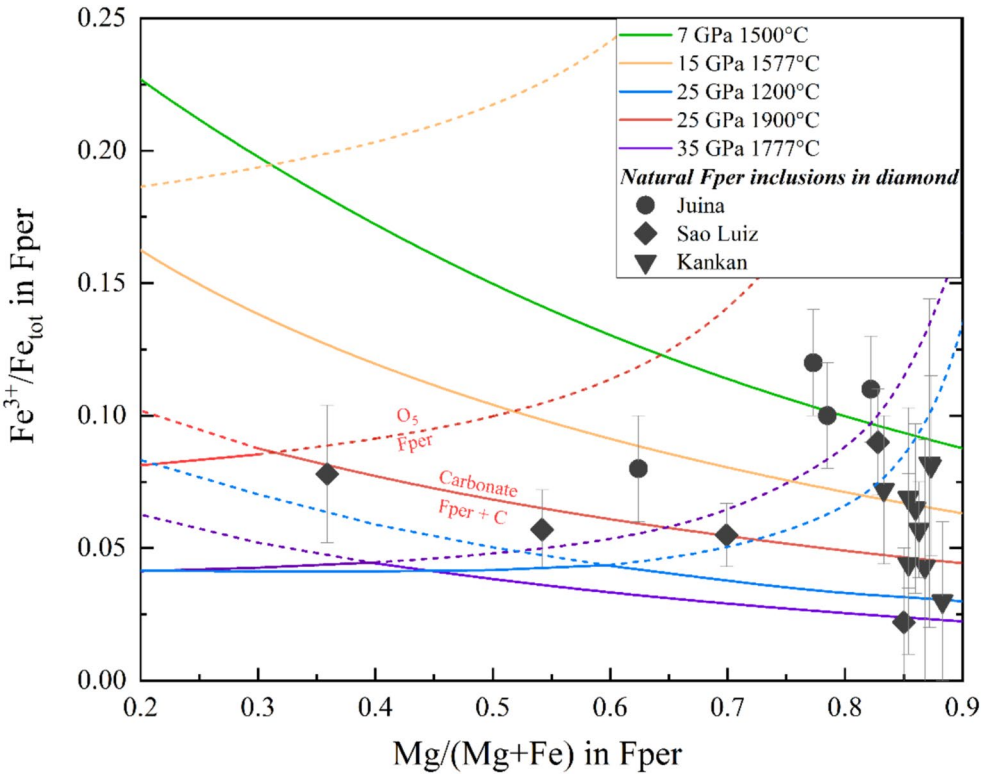


Fig. 12 The maximum Fe^{3+}/Fe_{tot} ratio of a fper inclusion in a diamond is calculated as a function of the fper Mg/(Mg+Fe) ratio at the conditions indicated by the colours of the curves. Along most of the solid curves, the Fe^{3+}/Fe_{tot} ratio in fper is limited by reaction of fper with diamond to form Fe–Mg carbonate solid solution. However, the mainly dashed curves indicate the limiting Fe^{3+}/Fe_{tot} ratio of fper where it reacts to form the O5 phase. At high pressure and high fper Mg/(Mg+Fe) ratio the two reactions cross and the maximum fper Fe^{3+}/Fe_{tot} ratio in diamond becomes limited by the reaction to form the O5 phase, indicated by the dashed curve becoming solid. Fe^{3+}/Fe_{tot} ratios reported for fper inclusions in natural diamonds are also plotted (Kaminsky et al. 2015). The fper inclusions cannot have formed at a particular set of P–T conditions if they plot above the corresponding solid curve

1900 °C) to demonstrate the effects of plausible subduction and plume temperatures at the top of the lower mantle. Dashed curves in Fig. 12 also show the Fe^{3+}/Fe_{tot} ratio of fper in equilibrium with the O5 phase. The curves for these two reactions cross at high pressures and at high fper Fe-contents. This indicates that the limit in fper stability in diamond becomes constrained not by the reaction to form carbonate but by the formation of the O5 phase, which is shown by a switch between the dashed and solid lines in Fig. 12.

The fO_2 of the FDM buffer increases with the Fe-content of fper, as does the equilibrium fper Fe^{3+}/Fe_{tot} ratio, but as all other components lower the FDM fO_2, the solid lines in Fig. 12 delineate the maximum Fe^{3+}/Fe_{tot} ratio that a fper inclusion in diamond can have for a given MgO content, P and T. This maximum fper Fe^{3+}/Fe_{tot} ratio decreases with P but increases with T. Stagno et al. (2011) reported an EELS measurement of 0.02 (±0.05) for the Fe^{3+}/Fe_{tot} ratio of $(Mg_{0.85}Fe_{0.15})O$ fper buffered by FDM at 45 GPa and 1700 °C. This is in excellent agreement with our FDM calculation, which predicts a ratio of 0.015 at the same conditions, providing a completely independent test of the model.

The decrease in the fper Fe^{3+}/Fe_{tot} ratio with pressure, which can be rationalised by the equilibrium

$$MgO_{(fper)} + C_{(diamond)} + 4FeO_{1.5(fper)} \leftrightarrow MgCO_{3(carbonate)} + 4FeO_{(fper)} \quad (12)$$

is very likely to continue further into the lower mantle as possible volume or stability changes such as resulting from phase transformations or Fe^{2+} high-spin to low-spin spin transitions (Badro et al. 2003; Isshiki et al. 2004) are only likely to affect the right-hand side of the equation. The only possible exception to this would be an Fe^{3+} electronic spin transition in ferropericlase, but to our knowledge no evidence of such a transition has ever been found.

Comparison with fper inclusions in natural diamonds

In Fig. 12, Fe^{3+}/Fe_{tot} ratios of fper inclusions in diamonds are plotted from three locations: the Juina kimberlites and the São Luiz placer deposit in Brazil and the Kankan placer deposit in Guinea, West Africa (Kaminsky et al. 2015). TEM studies reveal the presence of n-spft exsolution in fper inclusions from São Luiz and Juina diamonds (Wirth et al. 2014; Kaminsky et al. 2015). Wirth et al. (2014) analysed submicron regions of exsolved spft within a fper inclusion and the calculated K_D(app) (Fig. 7) is consistent with equilibration as the diamonds cooled near the Earth's surface. Wirth et al. (2014) corrected the reported MS Fe^{3+}/Fe_{tot} ratio of 0.070(26) for this inclusion (McCammon et al. 1997), to account for the estimated 6–11 vol.% of exsolved spft phase

and obtained a pre-exsolution fper Fe^{3+}/Fe_{tot} ratio of 0.11–0.14. Kaminsky et al. (2015) considered that the proportion of spft exsolution in fper inclusions could be generalised as 3.64 vol.% and determined that the MS fper Fe^{3+}/Fe_{tot} ratios should all be raised by 0.021 to account for this exsolution. While this may underestimate the effect of the exsolution, considering the results of Wirth et al. (2014), values corrected in this way are plotted in Fig. 12.

If we knew independently the P and T at which a specific fper inclusion formed, then using our model (provided in an Excel spreadsheet in the supplementary information) we could calculate the fO_2 from the fper Fe^{3+}/Fe_{tot} ratio. Such independent constraints are rarely available, however, but as the fper Fe^{3+}/Fe_{tot} ratio at FDM decreases with pressure, we can also place constraints on conditions that such inclusions could not have formed at, because their Fe^{3+}/Fe_{tot} ratios are too high. If the diamonds in which fper inclusions are found formed by reduction of solid Fe–Mg carbonates, then the FDM curves in Fig. 12 indicate the Fe^{3+}/Fe_{tot} ratio that a fper inclusion would have if it formed at the specified P, T condition. It is quite likely, however, that diamonds form from carbon-bearing fluids or melts and not from solid carbonates (Stagno et al. 2013). If so, for a given set of P–T conditions, this could only occur at oxygen fugacities lower than FDM, which would result in fper Fe^{3+}/Fe_{tot} ratios that plot below the FDM curves. The curves, therefore, indicate the highest plausible Fe^{3+}/Fe_{tot} ratio that a fper inclusion can have, if it formed at the P, T conditions specified.

For example, four of the samples from São Luiz and about half of the samples from Kankan could have formed from carbonate in the lower mantle, as they plot within error or below the FDM curve at 1900 °C and 25 GPa. However, if these samples were produced at oxygen fugacities lower than FDM buffer, which is more likely, then they could have been produced at practically any pressure up to lower mantle conditions. Consequently, low Fe^{3+}/Fe_{tot} ratio inclusions do not provide meaningful constraints on depth of origin because they may have formed anywhere within the diamond stability field at sufficiently low oxygen fugacity. Conversely, only fper inclusions with sufficiently low Fe^{3+}/Fe_{tot} ratios (≤ 0.05) are compatible with lower mantle formation. However, Fig. 12 indicates that the majority of the fper inclusions so far analysed have Fe^{3+}/Fe_{tot} ratios that are too high for them to have formed in the lower mantle, because their Fe^{3+} contents indicate oxygen fugacities greater than FDM at lower mantle conditions. Many of the samples from Kankan, for example, have Fe^{3+}/Fe_{tot} ratios that are above the FDM curve plotted for 25 GPa and, therefore, could only have formed at lower pressures, either in the transition zone or upper mantle. They could not have formed deeper, as their Fe^{3+} contents would be too high to be compatible with the diamond stability field. Such depths are consistent with studies using other geobarometric methods (Anzolini et al. 2019). Furthermore, the three Mg-rich samples from Juina that have Fe^{3+}/Fe_{tot} ratios ≥ 0.1 have a maximum possible depth of formation consistent with the base of the cratonic lithosphere. In fact, given that the graphite-diamond transition is near 5 GPa, these fper inclusions could only have been formed at oxygen fugacities close to the FDM buffer at or very near to cratonic lithosphere conditions.

As discussed previously, in the thermodynamic model optimisation, differences in independently determined oxygen fugacities for each experiment were generally <0.5 log units, although there were some larger outliers. This would equate to uncertainties in model–determined Fe^{3+}/Fe_{tot} ratios in Fig. 12 that are small in comparison to those of the natural samples. However, absolute uncertainties in the model oxygen fugacities are much harder to constrain. If the pressure dependences of the Fe-Pt interaction parameters proposed by Hirschmann and Zhang (2023) were employed, oxygen fugacities would decrease by up to 2.5 log units at 30 GPa and 1200 °C, as previously stated. Although it was not possible to successfully optimize the model using such a value, it is still worth considering the consequences of this potential uncertainty. This lower fO_2 value would equate to an increase in the $(Mg_{0.8}Fe_{0.2})_XO$ fper Fe^{3+}/Fe_{tot} ratio at 30 GPa and 1200 °C by approximately 0.05 for the FDM calculation in Fig. 12. At lower pressures the differences would be smaller.

However, although further work is required to better cross-calibrate high-pressure redox buffers, the excellent agreement between the calculated FDM fper Fe^{3+}/Fe_{tot} ratios and the independently determined value reported by Stagno et al. (2011) at 45 GPa, which was not used in the model refinement, provides an important independent validation of the model. Furthermore, although experimentally determined fper Fe^{3+}/Fe_{tot} ratios commonly carry significant uncertainties due to exsolution during quenching and the necessity to rely on EELS measurements, the thermodynamic model is not constrained by Fe^{3+}/Fe_{tot} ratios alone. The model simultaneously reproduces three independent observations: fper Fe^{3+}/Fe_{tot} ratios, oxygen fugacity determinations, and Fe–Mg partitioning behaviour. The combined reproduction of these datasets places strong constraints on the P–T evolution of the Fe^{3+}/Fe_{tot} ratio predicted by the model.

The tendency to assume that fper inclusions formed in the lower mantle arises from the fact that within typical mantle peridotite bulk compositions, fper is only stable at these depths. Several studies have proposed, however, that fper may be produced as shallower depths through the reduction of carbonates, within assemblages that are out of equilibrium with typical mantle rocks (Brey et al. 2004; Thomson et al. 2016; Bataleva et al. 2016; Bulatov et al. 2019). In fact, in a few instances, the diamonds containing the fper inclusions also contain carbonates (McCammon et al. 1997). An appealing

aspect of carbonate reduction is that it provides a mechanism to explain the high Fe-contents of some fper inclusions (Bulatov et al. 2019). Fe partitions strongly into fper in equilibrium with solid and liquid carbonates (Bulatov et al. 2019). The model shown in Fig. 11, for example, indicates that at 6 GPa and 1400 °C, fper with an Mg/(Mg+Fe) of 0.35 can be produced from partial reduction of a Ca-free carbonate with an Mg/(Mg+Fe) ratio of 0.93, although for formation from carbonate liquids the Fe fractionation would be less extreme. The reduction itself could have been a response to an influx of reduced CH_4 or H_2 bearing fluids. The surrounding mantle rocks themselves contain insufficient Fe^{2+} to reduce the significant quantities of carbonate that would be required to produce a macroscopic diamond (Luth and Stachel 2014).

Another scenario would be that diamonds are produced from H_2O-dominated melts that experiments show are also Mg and Fe-rich (Kawamoto and Holloway 1997; Nakajima et al. 2019). They may crystallise to form fper, especially if they had gone through several cycles of partial melting, migration and crystallisation, without re-equilibrating with typical mantle rocks. This could result from the thermal perturbation around a plume. Such H_2O-rich melts could form diamonds through a reaction such as, $CH_4+MgCO_3=2C+2H_2O+MgO$. Such a melt would have an fO_2 of at least 1 log unit below FDM (Stagno and Frost 2010). For any set of conditions, this would lower the fper Fe^{3+}/Fe_{tot} ratio by approximately half the value indicated for FDM in Fig. 12, which would imply that the majority of the natural inclusions would be consistent with formation in the cratonic lithosphere or at the top of the transition zone.

Based on crystallographic relationships, recent studies have proposed that some Mg-rich fper inclusions may be protogenetic (Lorenzon et al. 2023; Ni et al. 2025) and might not therefore reflect the conditions of diamond formation itself. However, unless encapsulation occurs extremely rapidly, protogenetic fper inclusions would at least partially re-equilibrate with the oxygen fugacity conditions associated with diamond formation. Even if rapid diamond growth allowed elevated protogenetic fper Fe^{3+}/Fe_{tot} ratios to initially be preserved, trapped fper inclusions with initially high Fe^{3+}/Fe_{tot} ratios would tend to react towards lower ferric iron contents consistent with equilibration with diamond at the conditions of entrapment. This would occur through redox reaction with the surrounding diamond, potentially producing post-entrapment carbonate within the inclusion. Due to the lack of another oxidising agent, post-entrapment modification could only lower rather than raise fper Fe^{3+}/Fe_{tot} ratios. Consequently, the upper oxygen fugacity limits defined here should still provide meaningful constraints on the conditions at which inclusions were trapped.

Formation conditions of a possible $[Mg,Fe]_3Fe_2O_6$ inclusion in a natural diamond

Kiseeva et al. (2022) reported Fe^{3+}/Fe_{tot} ratios for five additional fper inclusions in diamonds from São Luiz. Four of these had Fe^{3+}/Fe_{tot} ratios below the detection limit (<0.03). However, single-crystal XRD measurements for two inclusions, SL82 and SL5_2, indicate the presence of coexisting spft and fper phases showing a specific crystallographic orientation relationship, with [111] of the spinel-structured phase parallel to [100] of the cubic phase. For SL82, which has an $Fe_{tot}/(Fe_{tot}+Mg)$ ratio of 0.81, the Mössbauer spectrum also resolved a ferric iron doublet associated with the spft phase, whereas for SL5_2 the ferric iron signal was too weak to resolve. If the spft phase in SL82 exsolved from fper after entrapment, as suggested by the crystallographic relationship, then based on the reported Mössbauer spectrum the original inclusion, before exsolution, would have had an Fe^{3+}/Fe_{tot} ratio of approximately 0.5. This is far too high to correspond to a fper inclusion in a diamond under any conditions but the composition and oxidation state are an excellent match to the O6 phase with the formula $(Mg_{0.33}Fe^{2+}_{0.67})_3Fe^{3+}_2O_6$. The comparatively high reported Mn content for this inclusion is also consistent with the low fper-O6 partition coefficient for Mn (Fig. 8b). As shown in Fig. 7, the K_D(app) for this inclusion is quite unlike that expected for fper-spft equilibrium, which can, however, be explained if both phases are actually formed through a decomposition of the O6 phase. The O6 phase was only observed experimentally in our study with $Fe^{2+}/(Mg+Fe^{2+})$ ratios>0.8 (Fig. 3; Table 2). However, at 1400 °C and 10 GPa Woodland et al. (2023) reported an O6 phase with an $Fe^{2+}/(Mg+Fe^{2+})$ ratio of 0.73, which is close to the value of 0.67 proposed here, consistent with an expansion of the O6 phase field, compared to O5, towards slightly higher temperatures. Therefore, it is highly likely that the fper and spft assemblage in inclusion SL82 formed through exsolution from an O6 phase that was the initial phase trapped in the diamond.

In Fig. 12 dashed curves denote the limit of fper stability with respect to the O5 phase and it can be seen that at high Fe-contents the FDM curves cross those that delimit the O5 stability at 25 GPa. Although this figure is conceived in terms of the fper Fe^{3+}/Fe_{tot} ratios, where curves calculated for the same conditions cross, the oxygen fugacites of the two equilibria are also identical. The implication is that the O5 phase can be in equilibrium with diamond at 25 GPa, at temperatures between 1200 °C and 1900 °C. Although we are not currently able to calculate the O6 stability field, it is very likely to form from the O5 phase at similar conditions (Woodland et al. 2023) and, therefore, can also be in equilibrium with diamond and carbonate. In fact the lower Fe^{3+}/Fe^{2+} ratio of the

O6 phase compared to O5 makes it more likely to be stable at diamond forming conditions (Myhill et al. 2016). It is interesting to note that if this O6 phase formed by the reduction of carbonate near the top of the lower mantle, then although it has a high Fe^{3+} content, its stability at these conditions would not require especially oxidising conditions, other than those required for carbonate stability. The formation of the O6 phase and diamond would be an inevitable consequence of the formation of a carbonate with a sufficiently high iron content and can be described by the end member reaction:

$$5FeCO_3 = Fe_5O_6 + 0.5C + 4.5CO_2 \quad (13)$$

where CO_2 would form more carbonate by reacting with other Mg or Ca components. Similar mechanisms involving either spft or other high-pressure oxides have been proposed as a diamond forming mechanism in both experimental and natural samples (Boulard et al. 2012; Cerantola et al. 2017; Chen et al. 2018). If the O6 phase formed at 25 GPa and 1700 °C, then employing the calculations shown in Fig. 11, the coexisting carbonate would need to have an Fe/(Fe+Mg) ratio of only 0.09, (although this value would be higher if the carbonate were Ca-bearing or liquid), and the fO_2 would be approximately 3.5 log units above IW.

Conclusions

Experiments on ferropericlase coexisting with spinel-ferrite to ~ 10 GPa and high-pressure $(Fe,Mg)_2Fe_2O_5$ (O5 phase) to 30 GPa, define the upper oxygen fugacity limit of ferropericlase stability and provide constraints on how ferropericlase Fe^{3+}/Fe_{tot} ratios vary with pressure, temperature and composition. Ferropericlase synthesized at high pressure commonly undergoes exsolution of nanocrystalline spinel-ferrite during quenching, which complicates the determination of ferropericlase Fe^{3+}/Fe_{tot} ratios from Mössbauer spectroscopy and influences the unit-cell parameters and possibly other physical properties measured on recovered samples.

A thermodynamic model for the Mg–Fe–O system was calibrated using experimental constraints on ferropericlase Fe^{3+}/Fe_{tot} ratios, oxygen fugacity and Fe–Mg partitioning between ferropericlase and coexisting Fe^{3+}-rich oxides. The model predicts that, at 1200 °C, the maximum Fe^{3+}/Fe_{tot} ratio of mantle-like ferropericlase increases to ~ 0.55 by 10 GPa, but then decreases sharply at higher pressures due to stabilisation of the O5 phase, reaching values < 0.05 by 30 GPa.

Calculations of the limiting fo_2 at diamond entrapment set by the formation of carbonates, show that very few ferropericlase inclusions analysed to date have Fe^{3+}/Fe_{tot} ratios low enough for them to have formed in the lower mantle. Most have maximum formation depths consistent with the transition zone and a few of the most Fe^{3+}-rich could have only formed in the upper mantle, possibly in the lithosphere, from oxidised precursors such as carbonates.

The stability fields of the O5 and $(Fe,Mg)_3Fe_2O_6$ (O6) phases converge towards oxygen fugacities relevant to diamond formation near the base of the transition zone and top of the lower mantle for Fe-rich bulk compositions. This implies that such high-pressure Fe^{3+}-rich oxides may occur as inclusions in natural diamonds. A previously reported composite inclusion of ferropericlase and spinel-ferrite (Kiseeva et al. 2022) is interpreted here as the back-transformation product of a trapped O6 high-pressure phase and is consistent with diamond formation from a moderately Fe-enriched carbonate.

Supplementary Information The online version contains supplementary material available at https://doi.org/10.1007/s00410-026-02341-w.

Acknowledgements The authors thank Raphael Njul for sample preparation and Detlef Krauße for assistance with EPMA analyses. We thank I Kupenko for sharing unpublished data on the Mössbauer spectrum of the $Mg_2Fe_2O_5$ phase. We gratefully appreciate the constructive comments of Kate Kiseeva, an anonymous reviewer and the Executive Editor Dante Canil, which significantly improved the original manuscript. This study was financed by the international research and training group Deep Earth Volatile Cycles DFG grant no. GRK 2156/1 and by DFG grant 1555/11. We acknowledge the DFG for funding of the FIB facility (Project number 257745926) and the TEM facility (Project number 189856261) at the Bayerisches Geoinstitut.

Funding Open Access funding enabled and organized by Projekt DEAL.

Data Availability The authors declare that the data supporting the findings of this study are available within the paper and its supplementary information files.

Open Access This article is licensed under a Creative Commons Attribution 4.0 International License, which permits use, sharing, adaptation, distribution and reproduction in any medium or format, as long as you give appropriate credit to the original author(s) and the source, provide a link to the Creative Commons licence, and indicate if changes were made. The images or other third party material in this article are included in the article's Creative Commons licence, unless indicated otherwise in a credit line to the material. If material is not included in the article's Creative Commons licence and your intended use is not permitted by statutory regulation or exceeds the permitted use, you will need to obtain permission directly from the copyright holder. To view a copy of this licence, visit http://creativecommons.org/licenses/by/4.0/.

References

Anzolini C, Nestola F, Mazzucchelli ML et al (2019) Depth of diamond formation obtained from single periclase inclusions. Geology 47:219–222. https://doi.org/10.1130/g45605.1

Anzolini C, Marquardt K, Stagno V et al (2020) Evidence for complex iron oxides in the deep mantle from FeNi(Cu) inclusions in

superdeep diamond. Proc Natl Acad Sci 117:21088–21094. https://doi.org/10.1073/pnas.2004269117

Armstrong K, Siersch NC, Boffa-Ballaran T et al (2020) Equations of state, phase relations, and oxygen fugacity of the Ru-RuO2 buffer at high pressures and temperatures. Am Mineral 105:333–343. https://doi.org/10.2138/am-2020-7060

Badro J, Fiquet G, Guyot F et al (2003) Iron partitioning in earth's mantle: toward a deep lower mantle discontinuity. Science 300:789–791. https://doi.org/10.1126/science.1081311

Bataleva YV, Palyanov YN, Borzdov YM et al (2016) Synthesis of diamonds with mineral, fluid and melt inclusions. Lithos 265:292–303. https://doi.org/10.1016/j.lithos.2016.07.005

Bolfan-Casanova N, Mackwell S, Keppler H et al (2002) Pressure dependence of H solubility in magnesiowüstite up to 25 GPa: Implications for the storage of water in the Earth's lower mantle. Geophys Res Lett. https://doi.org/10.1029/2001GL014457

Boulard E, Menguy N, Auzende AL et al (2012) Experimental investigation of the stability of Fe-rich carbonates in the lower mantle. J Geophys Res Solid Earth. https://doi.org/10.1029/2011jb008733

Brey GP, Bulatov V, Girnis A et al (2004) Ferropericlase—a lower mantle phase in the upper mantle. Lithos 77:655–663. https://doi.org/10.1016/j.lithos.2004.03.013

Brynestad J, Flood H (1958) The Redox Equilibrium in Wüstite and Solid Solutions of Wüstite and Magnesium Oxide. Z Für Elektrochem Berichte Bunsenges Für Phys Chem 62:953–958. https://doi.org/10.1002/bbpc.19580620905

Bulatov VK, Girnis AV, Brey GP et al (2019) Ferropericlase crystallization under upper mantle conditions. Contrib Mineral Petrol 174:45. https://doi.org/10.1007/s00410-019-1582-6

Campbell AJ, Danielson L, Righter K et al (2009) High pressure effects on the iron–iron oxide and nickel–nickel oxide oxygen fugacity buffers. Earth Planet Sci Lett 286:556–564. https://doi.org/10.1016/j.epsl.2009.07.022

Castellanos-Rubio I, Rodrigo I, Munshi R et al (2019) Outstanding heat loss via nano-octahedra above 20 nm in size: from wustite-rich nanoparticles to magnetite single-crystals. Nanoscale. https://doi.org/10.1039/C9NR04970C

Cerantola V, Bykova E, Kupenko I et al (2017) Stability of iron-bearing carbonates in the deep Earth's interior. Nat Commun. https://doi.org/10.1038/ncomms15960

Chen M, Shu J, Xie X et al (2018) Natural diamond formation by self-redox of ferromagnesian carbonate. Proc Natl Acad Sci 115:2676–2680. https://doi.org/10.1073/pnas.1720619115

Dimitrov DV, Unruh K, Hadjipanayis GC et al (1999) Ferrimagnetism and defect clusters in Fe 1–x O films. Phys Rev B 59:14499–14504. https://doi.org/10.1103/PhysRevB.59.14499

Dobson D, Cohen N, Pankhurst Q, Brodholt J (1998) A convenient method for measuring ferric iron in magnesiowustite (MgO-Fe1-xO). Am Mineral 83:794–798

Dorogokupets PI, Dymshits AM, Litasov KD, Sokolova TS (2017) Thermodynamics and Equations of State of Iron to 350 GPa and 6000 K. Sci Rep 7:41863. https://doi.org/10.1038/srep41863

Frost DJ (2003) The structure and sharpness of (Mg,Fe)2SiO4 phase transformations in the transition zone. Earth Planet Sci Lett 216:313–328. https://doi.org/10.1016/S0012-821X(03)00533-8

Goya GF, Berquó TS, Fonseca FC, Morales MP (2003) Static and dynamic magnetic properties of spherical magnetite nanoparticles. J Appl Phys 94:3520–3528. https://doi.org/10.1063/1.1599959

Gurney JJ (1989) Diamonds. In: Ross J (ed) Kimberlites and Related Rocks: Their composition, occurrence, origin and emplacement. Published for Blackwell Scientific Publications for the Geological Society of Australia Incorporated, Victoria, pp 935–965

Harte B (1994) Lower mantle mineral associations preserved in diamonds. Mineral Mag 58A:384–385. https://doi.org/10.1180/minmag.1994.58A.1.201

Harte B, Harris JW, Hutchison MT et al (1999) Lower mantle mineral associations in diamonds from São Luiz, Brazil. In: Fei Y, Bertka CM, Mysen BO (eds) Mantle Petrology: Field Observations and High Pressure Experimentation, A Tribute to Francis R (Joe) Boyd. Geochemical Society, Houston, pp 125–153

Hartridge A, Bhattacharya AK, Sengupta M et al (1997) Crystallite size dependence on the magnetic properties of nanocrystalline magnetite powders. J Magn Magn Mater 176:L89–L92. https://doi.org/10.1016/S0304-8853(97)01004-4

Hazen RM, Jeanloz R (1984) Wüstite (Fe_{1-x} O): a review of its defect structure and physical properties. Rev Geophys 22:37–46. https://doi.org/10.1029/RG022i001p00037

Hidayat T, Shishin D, Jak E, Decterov SA (2015) Thermodynamic reevaluation of the Fe–O system. Calphad 48:131–144. https://doi.org/10.1016/j.calphad.2014.12.005

Hilbrandt N, Martin M (1998) High temperature point defect equilibria in iron-doped MgO: an *in situ* Fe-K XAFS study on the valence and site distribution of iron in (Mg_{1-x} Fe_x)O. Ber Bunsenges Phys Chem 102:1747–1759. https://doi.org/10.1002/bbpc.19981021204

Hirschmann MM (2021) Iron-wüstite revisited: a revised calibration accounting for variable stoichiometry and the effects of pressure. Geochim Cosmochim Acta 313:74–84. https://doi.org/10.1016/j.gca.2021.08.039

Hirschmann MM, Zhang HL (2023) A revised model for activity–composition relations in solid and molten FePt alloys and a preliminary model for characterization of oxygen fugacity in high-pressure experiments. Eur J Mineral 35:789–803. https://doi.org/10.5194/ejm-35-789-2023

Holland TJB, Powell R (2011) An improved and extended internally consistent thermodynamic dataset for phases of petrological interest, involving a new equation of state for solids. J Metamorph Geol 29:333–383. https://doi.org/10.1111/j.1525-1314.2010.00923.x

Ishii T, Yamazaki D, Tsujino N et al (2017) Pressure generation to 65 GPa in a Kawai-type multi-anvil apparatus with tungsten carbide anvils. High Press Res 37:507–515. https://doi.org/10.1080/08957959.2017.1375491

Ishii T, Uenver-Thiele L, Woodland AB et al (2018) Synthesis and crystal structure of Mg-bearing Fe9O11: New insight in the complexity of Fe-Mg oxides at conditions of the deep upper mantle. Am Mineral 103:1873–1876. https://doi.org/10.2138/am-2018-6646

Isshiki M, Irifune T, Hirose K et al (2004) Stability of magnesite and its high-pressure form in the lowermost mantle. Nature 427:60–63. https://doi.org/10.1038/nature02181

Jung I-H, Decterov SA, Pelton AD (2004) Critical thermodynamic evaluation and optimization of the Fe–Mg–O system. J Phys Chem Solids 65:1683–1695. https://doi.org/10.1016/j.jpcs.2004.04.005

Kaminsky F (2012) Mineralogy of the lower mantle: A review of 'super-deep' mineral inclusions in diamond. Earth-Sci Rev 110:127–147. https://doi.org/10.1016/j.earscirev.2011.10.005

Kaminsky F, Zakharchenko O, Davies R et al (2001) Superdeep diamonds from the Juina area, Mato Grosso State, Brazil. Contrib Mineral Petrol 140:734–753. https://doi.org/10.1007/s004100000221

Kaminsky FV, Ryabchikov ID, McCammon CA et al (2015) Oxidation potential in the Earth's lower mantle as recorded by ferropericlase inclusions in diamond. Earth Planet Sci Lett 417:49–56. https://doi.org/10.1016/j.epsl.2015.02.029

Kang N, Schmidt MW, Poli S et al (2016) Melting relations in the system FeCO3–MgCO3 and thermodynamic modelling of Fe–Mg

carbonate melts. Contrib Mineral Petrol 171:74. https://doi.org/10.1007/s00410-016-1283-3
Katsura T (2022) A revised adiabatic temperature profile for the mantle. J Geophys Res Solid Earth 127:e2021JB023562. https://doi.org/10.1029/2021JB023562
Katsura T, Kimura S (1965) Equilibria in the System FeO–Fe2O3–MgO at 1160°C. Bull Chem Soc Jpn 38:1664–1670. https://doi.org/10.1246/bcsj.38.1664
Kawamoto T, Holloway JR (1997) Melting temperature and partial melt chemistry of H $_2$ O-saturated mantle peridotite to 11 gigapascals. Science 276:240–243. https://doi.org/10.1126/science.276.5310.240
Keppler H, Frost DJ (2005) Introduction to minerals under extreme conditions. In: Papp G, Weiszburg TG, Miletich R (eds) Mineral behaviour at extreme conditions. Mineralogical society of Great Britain and Ireland, London, pp 1–30
Kessel R, Beckett JR, Stolper EM (2001) Thermodynamic properties of the Pt-Fe system. Am Mineral 86:1003–1014. https://doi.org/10.2138/am-2001-8-907
Kiseeva ES, Korolev N, Koemets I et al (2022) Subduction-related oxidation of the sublithospheric mantle evidenced by ferropericlase and magnesiowüstite diamond inclusions. Nat Commun 13:7517. https://doi.org/10.1038/s41467-022-35110-x
Koch F, Cohen JB (1969) The defect structure of Fe1−xO. Acta Crystallogr B 25:275–287. https://doi.org/10.1107/S0567740869002111
Larson CA, von Dreele R (2004) General structure analysis system (GSAS)
Lavina B, Meng Y (2015) Unraveling the complexity of iron oxides at high pressure and temperature: Synthesis of Fe_5O_6. Sci Adv 1:e1400260. https://doi.org/10.1126/sciadv.1400260
Lavina B, Dera P, Kim E et al (2011) Discovery of the recoverable high-pressure iron oxide Fe_4O_5. Proc Natl Acad Sci 108:17281–17285. https://doi.org/10.1073/pnas.1107573108
Long GJ, Cranshaw TE, Longworth G (1983) The ideal Mössbauer effect absorber thickness. Mössbauer Eff Ref Data J 6:42–29
Longo M, McCammon CA, Jacobsen SD (2011) Microanalysis of the iron oxidation state in (Mg,Fe)O and application to the study of microscale processes. Contrib Mineral Petrol 162:1249–1257. https://doi.org/10.1007/s00410-011-0649-9
Lorenzon S, Wenz M, Nimis P et al (2023) Dual origin of ferropericlase inclusions within super-deep diamonds. Earth Planet Sci Lett 608:118081. https://doi.org/10.1016/j.epsl.2023.118081
Luth RW, Stachel T (2014) The buffering capacity of lithospheric mantle: implications for diamond formation. Contrib Mineral Petrol. https://doi.org/10.1007/s00410-014-1083-6
McCammon C, Hutchison M, Harris J (1997) Ferric Iron Content of Mineral Inclusions in Diamonds from São Luiz: A View into the Lower Mantle. Science 278:434–436. https://doi.org/10.1126/science.278.5337.434
McCammon C, Peyronneau J, Poirier J (1998) Low ferric iron content of (Mg,Fe)O at high pressures and temperatures. Geophys Res Lett 25:1589–1592. https://doi.org/10.1029/98GL01178
McCammon CA, Lauterbach S, Seifert F et al (2004) Iron oxidation state in lower mantle mineral assemblages. Earth Planet Sci Lett 222:435–449. https://doi.org/10.1016/j.epsl.2004.03.018
Melai C, Boffa Ballaran T, Uenver-Thiele L et al (2023) Compressibilities along the magnetite–magnesioferrite solid solution. Phys Chem Miner 50:1. https://doi.org/10.1007/s00269-022-01217-2
Melai C, Boffa Ballaran T, Neri A et al (2026) The periclase -wüstite stability field and the exsolution of coherent nano-crystalline spinel ferrite at one atmosphere. Am Mineral. https://doi.org/10.2138/am-2025-9930
Myhill R, Ojwang DO, Ziberna L et al (2016) On the P-T– $$fO_{2}$$ f O 2 stability of Fe4O5, Fe5O6 and Fe4O5-rich solid solutions. Contrib Mineral Petrol 171:51. https://doi.org/10.1007/s00410-016-1258-4
Nakajima A, Sakamaki T, Kawazoe T, Suzuki A (2019) Hydrous magnesium-rich magma genesis at the top of the lower mantle. Sci Rep 9:. https://doi.org/10.1038/s41598-019-43949-2
Nestola F, Cerantola V, Milani S et al (2016) Synchrotron Mössbauer Source technique for in situ measurement of iron-bearing inclusions in natural diamonds. Lithos 265:328–333. https://doi.org/10.1016/j.lithos.2016.06.016
Ni P, Shirey SB, Walter MJ et al (2025) Onset of slab mantle melting in Earth's lower mantle: evidence from ferropericlase in superdeep diamonds. Sci Adv 11:eadt9106. https://doi.org/10.1126/sciadv.adt9106
Nimis P, Nestola F, Schiazza M et al (2019) Fe-rich ferropericlase and magnesiowüstite inclusions reflecting diamond formation rather than ambient mantle. Geology 47:27–30. https://doi.org/10.1130/G45235.1
O'Neill HStC, Pownceby MI, McCammon CA (2003) The magnesiowüstite: iron equilibrium and its implications for the activity-composition relations of (Mg,Fe)2SiO4 olivine solid solutions. Contrib Mineral Petrol 146:308–325. https://doi.org/10.1007/s00410-003-0496-4
Otsuka K, McCammon CA, Karato S (2010) Tetrahedral occupancy of ferric iron in (Mg,Fe)O: Implications for point defects in the Earth's lower mantle. Phys Earth Planet Inter 180:179–188. https://doi.org/10.1016/j.pepi.2009.10.005
Otsuka K, Longo M, McCammon CA, Karato S (2013) Ferric iron content of ferropericlase as a function of composition, oxygen fugacity, temperature and pressure: Implications for redox conditions during diamond formation in the lower mantle. Earth Planet Sci Lett 365:7–16. https://doi.org/10.1016/j.epsl.2012.11.030
Ovsyannikov SV, Bykov M, Bykova E et al (2018) Pressure tuning of charge ordering in iron oxide. Nat Commun 9:4142. https://doi.org/10.1038/s41467-018-06457-x
Palot M, Jacobsen SD, Townsend JP et al (2016) Evidence for H2O-bearing fluids in the lower mantle from diamond inclusion. Lithos 265:237–243. https://doi.org/10.1016/j.lithos.2016.06.023
Prescher C, McCammon C, Dubrovinsky L (2012) *MossA* : a program for analyzing energy-domain Mössbauer spectra from conventional and synchrotron sources. J Appl Crystallogr 45:329–331. https://doi.org/10.1107/S0021889812004979
Scott Smith BH, Danchin RV, Harris JW, Stracke KJ (1984) Kimberlites Near Orroroo, South Australia. In: Kornprobst J (ed) Developments in Petrology. Elsevier, pp 121–142
Sinmyo R, Bykova E, Ovsyannikov SV et al (2016) Discovery of Fe7O9: a new iron oxide with a complex monoclinic structure. Sci Rep 6:32852. https://doi.org/10.1038/srep32852
Speidel DH (1967) Phase Equilibria in the System MgO-FeO-Fe2 O3: The 1300°C Isothermal Section and Extrapolations to Other Temperatures. J Am Ceram Soc 50:243–248. https://doi.org/10.1111/j.1151-2916.1967.tb15096.x
Srečec I, Ender A, Woermann E et al (1987) Activity-composition relations of the magnesiowüstite solid solution series in equilibrium with metallic iron in the temperature range 1050–1400 K. Phys Chem Miner 14:492–498. https://doi.org/10.1007/BF00308284
Stachel T, Harris JW, Brey GP (1998) Rare and unusual mineral inclusions in diamonds from Mwadui, Tanzania. Contrib Mineral Petrol 132:34–47. https://doi.org/10.1007/s004100050403
Stachel T, Harris JW, Brey GP, Joswig W (2000) Kankan diamonds (Guinea) II: lower mantle inclusion parageneses. Contrib Mineral Petrol 140:16–27. https://doi.org/10.1007/s004100000174
Stagno V, Frost DJ (2010) Carbon speciation in the asthenosphere: Experimental measurements of the redox conditions at which carbonate-bearing melts coexist with graphite or diamond in

peridotite assemblages. Earth Planet Sci Lett 300:72–84. https://doi.org/10.1016/j.epsl.2010.09.038

Stagno V, Tange Y, Miyajima N et al (2011) The stability of magnesite in the transition zone and the lower mantle as function of oxygen fugacity. Geophys Res Lett 38:n/a-n/a. https://doi.org/10.1029/2011gl049560

Tange Y, Nishihara Y, Tsuchiya T (2009) Unified analyses for P-V-T equation of state of MgO: a solution for pressure-scale problems in high P-T experiments. J Geophys Res Solid Earth 114:2008JB005813. https://doi.org/10.1029/2008JB005813

Thomson AR, Walter MJ, Kohn SC, Brooker RA (2016) Slab melting as a barrier to deep carbon subduction. Nature 529:76–79. https://doi.org/10.1038/nature16174

Toby BH (2001) EXPGUI, a graphical user interface for GSAS. J Appl Crystallogr 34:210–213. https://doi.org/10.1107/S0021889801002242

Uenver-Thiele L, Woodland AB, Ballaran TB et al (2017) Phase relations of Fe-Mg spinels including new high-pressure post-spinel phases and implications for natural samples. Am Mineral 102:2054–2064. https://doi.org/10.2138/am-2017-6119

Walter MJ, Thomson AR, Smith EM (2022) Geochemistry of silicate and oxide inclusions in sublithospheric diamonds. Rev Mineral Geochem 88:393–450. https://doi.org/10.2138/rmg.2022.88.07

Wirth R, Dobrzhinetskaya L, Harte B et al (2014) High-Fe (Mg, Fe) O inclusion in diamond apparently from the lowermost mantle. Earth Planet Sci Lett 404:365–375. https://doi.org/10.1016/j.epsl.2014.08.010

Woodland AB, O'Neill HStC (1997) Thermodynamic data for Fe-bearing phases obtained using noble metal alloys as redox sensors. Geochim Cosmochim Acta 61:4359–4366. https://doi.org/10.1016/S0016-7037(97)00247-0

Woodland AB, Frost DJ, Trots DM et al (2012) In situ observation of the breakdown of magnetite (Fe3O4) to Fe4O5 and hematite at high pressures and temperatures. Am Mineral 97:1808–1811. https://doi.org/10.2138/am.2012.4270

Publisher's Note Springer Nature remains neutral with regard to jurisdictional claims in published maps and institutional affiliations.